# Fringe Fields and Dynamic Aperture in Muon Storage Rings

F. Zimmermann, C. Johnstone, M. Berz, B. Erdelyi, K. Makino, W. Wan

March 3, 2000

**Abstract**

Quadrupole fringe fields can limit the dynamic aperture of muon storage rings. Using the computer code COSY INFINITY for particle tracking and normal-form analysis, we evaluate the importance of the fringe fields, and identify regions in the rings where they are critical. Dynamic aperture and linear tune shifts with amplitude are calculated, considering ideal machines without any errors or misalignments. We also study the efficiency of various nonlinear correction schemes, and we evaluate the spin decoherence over the transverse phase space. Results are presented for two muon storage ring optics, developed at FNAL and at CERN.

# 1 Introduction

In this paper, we investigate the effect of fringe fields in the muon storage ring of a neutrino factory, continuing earlier studies by M. Berz, K. Makino and B. Erdelyi [1]. The muons only have to be stored for a few hundred turns. Nevertheless, fringe fields are important because the beam fills almost the entire magnet aperture. The transverse normalized beam emittance in the FNAL muon storage ring is 3.2 mm mrad. At 50 GeV, this corresponds to a geometric emittance of about 7 $\mu$m, or to beam sizes of a few centimeters. The rms energy spread of 1% rms is also significant. An acceptance of $\pm 3\sigma$ for a few hundred turns is required both in transverse phase space and in momentum.

The FNAL ring optics consists of two arcs separated by two straight sections [2]. One of the straight sections is used for neutrino production. Here, the magnets are weakly focusing and the beta functions are large in order to confine the beam divergence. The return straight on the opposite side of the ring exhibits stronger focusing and much smaller beta functions. The magnet apertures vary roughly with the beam size. Quadrupole bore radii are 17 cm in the productiuon straight, 9 cm in the return straight and 7 cm in the arcs. Pole tip fields are 0.05 T, 0.84 T, and 3.6 T, respectively, and quadrupole lengths 3 m in the production sraight and 1 m elsewhere. The arcs are equipped with sextupoles for chromatic correction. Table 1 summarises the relevant parameters. The parameter $\eta_{\rm prod}$ in the table refers to the fraction of muons decaying in the production straight. The exponential decay time of the muons corresponds to about 180 turns.

Figure 2 illustrates the field fall-off near a magnet edge, as assumed in the default fringe-field calculation of COSY INFINITY [3, 4]: The variation of a dipole or quadrupole field with longitudinal position $z$ is represented by an Enge function of the form

$$F(z) = \frac{1}{1+\exp(a_1 + a_2(z/D) + \ldots + a_6(z/D)^6)} \tag{1}$$

where $D$ denotes the magnet full aperture, and the $a_i$ $(i = 1, \ldots, 6)$ are known as Enge coefficients. The standard Enge coefficients represent measurements of a family of PEP magnets [5].

# 2 Tracking Results for the FNAL Muon Storage Ring

A COSY input file of the muon storage ring was created from the MAD lattice [6] using the MAD-to-COSY converter [7]. The fractional betatron tunes computed by COSY are $\nu_x = 0.6229$, and $\nu_y = 0.3158$. The ring contains three different types of nonlinearities: fringes, sextupoles and kinematic corrections.

Table 1: Some parameters of the muon storage ring. † $r_p = 17$ cm in our tracking study

| | | |
|---|---|---|
| beam energy | $E$ | 50 GeV |
| normalized emittance | $\gamma\epsilon_{x,y}$ | 3.2 mm mrad |
| rms energy spread | $(\Delta p/p)_{\rm rms}$ | 1% |
| circumference | $C$ | 1752 m |
| neutrino decay fraction | $\eta_{\rm prod}$ | 39.2% |
| betatron tunes | $\nu_{x,y}$ | 13.63, 13.31 |
| arc quad radius | $r_a$ | 7 cm |
| arc quad pole tip | $B_{T,a}$ | 3.6 T |
| arc quad length | $l_a$ | 1 m |
| arc dipole field | $B$ | 6 T |
| arc dipole length | $l$ | 2.4 m |
| production quad radius | $r_p$ | 16.5 cm† |
| production quad pole tip | $B_{T,p}$ | 0.05 T |
| production quad length | $l_p$ | 1 m |
| return quad radius | $r_r$ | 9 cm |
| return quad pole tip | $B_{T,r}$ | 0.84 T |
| return quad length | $l_r$ | 1 m |

Figure 3 shows the horizontal and vertical phase space obtained by tracking for 1000 turns (trajectories are plotted on every 5th turn) through a 9th order Taylor map representing the bare ring without fringes and without sextupoles. The vertical axis is the horizontal or vertical slope of the particle trajectory, $x'$ or $y'$, in units of rad, and the horizontal axis is the transverse position, $x$ or $y$, in units of meter. The observation point is at the center of a defocusing quadrupole in the return straight. In Fig. 3, the only nonlinearity are kinematic terms, and the dynamic aperture is far outside the range of the plot, which extends over $\pm 4\sigma$. Figure 4 depicts similar tracking results including the chromatic-correction sextupoles, but still without any fringe fields. This is the situation normally considered in most tracking codes. The dynamic aperture is well above the required $3\sigma$. Figure 5 shows the phase space calculated by MAD for the same conditions (but trajectories are plotted on every turn). We ascribe differences at large amplitudes to the truncation of the COSY Taylor map.

The dramatic effect of the fringe fields is illustrated in Fig. 6, which depicts the phase space with both sextupoles and fringe fields. The tracking was performed using an option of COSY which automatically corrects the linear effect of the fringe fields (such as tune shift), so that we only study the influence of the nonlinear terms. The plot range in Fig. 6 again covers $\pm 4\sigma$. The dynamic aperture is about $2.5\sigma_x$ in the horizontal plane, and 1.5–$2\sigma_y$ vertically.

An analytical estimate of the fringe field effect indicates that the linear tune shift induced by quadrupole fringes scales as $\beta_{Q;x,y}^2 K_q^2 l_Q$, where $K_Q$ is the quadrupole gradient in units of inverse square meters, $l_Q$ the quadrupole length and $\beta_Q$ the beta function at the quadrupole [8]. Guided by this dependence, we discovered that a large portion of the fringe effect is due to two groups of three or four strong matching quadrupoles (QFF2, QDD2, QMF1, QMD1) which are located between arcs and production straight. The field gradient in these magnets is up to 500 times higher than the quadrupole gradient in the production straight proper, while the beta functions are of comparable size. Since the magnets are short, we expect that their length could be increased with appropriate optics rematching. For now, we simply switch off the fringe fields for these four magnets, and repeat the previous tracking calculations.

Figure 7 shows the phase space when we ignore the fringe field effects in the matching quadrupoles. Fringe fields are still taken into account for all the other quadrupoles. The dynamic aperture is now about the same as that caused by sextupoles alone; compare Fig. 4. Thus, we are confident that rematching the two arc-straight transitions using weaker quadrupoles will eliminate the fringe-field problem.

The tracking accuracy increases with the order of the Taylor map. To examine this dependence, we have tracked through maps of various order representing the most nonlinear case with both sextupoles and fringe fields included. Figures 8 and 9 show the phase space obtained by tracking through 11th and 7th order, respectively. The dynamic aperture for the 11th order map is almost the same as for the 9th order plot in

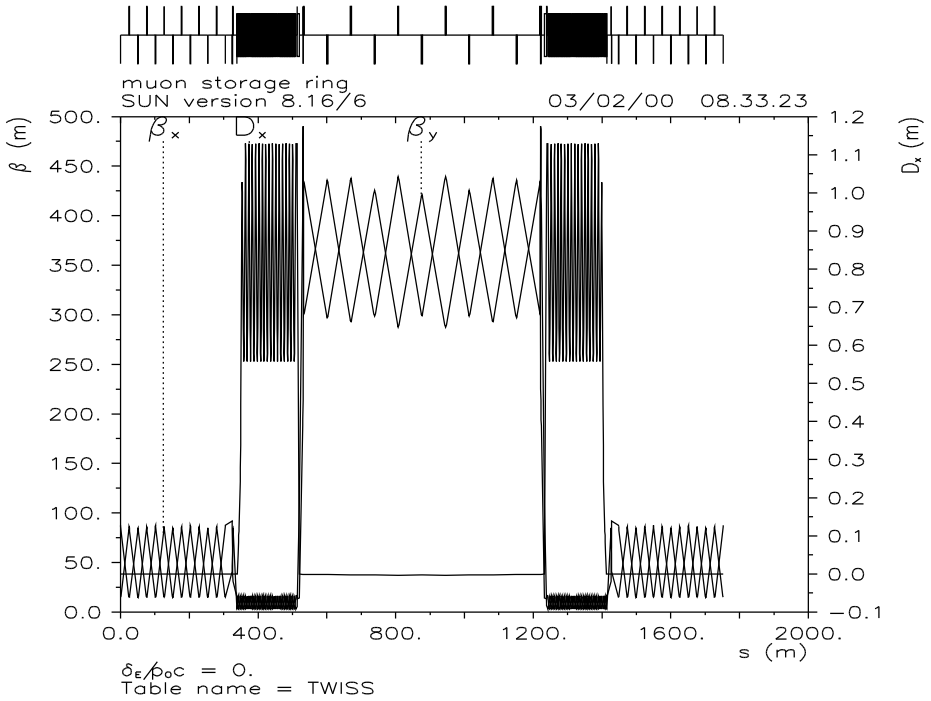


Figure 1: Optics of the FNAL muon storage ring [2].

Table 2: Linear tune shift in various configurations. The bare lattice contains kinematic terms only.

| tune shift | $d\nu_x/dI_x$ | $d\nu_x/dI_y$ | $d\nu_y/dI_y$ |
|---|---|---|---|
| sexts. & all fringes | 1376 | 2098 | 1570 |
| sexts. & fringes w/o matching section | 106 | −436 | 82 |
| all fringes, no sexts. | 1440 | 2674 | 1652 |
| fringes w/o matching section, no sexts. | 168 | 180 | 146 |
| sexts. only | −4 | −558 | 0.6 |
| bare lattice | 60 | 32 | 40 |

Fig. 6. For the 7th order map, the dynamic aperture is reduced in both planes. This suggests that the 7th order calculation is not sufficient for the amplitude and turn range of interest. Thus, most phase space plots in this report were created using maps of order 9 or higher.

The tune shifts with amplitude can be obtained from a COSY normal form analysis. Specifically, the linear tune shift $d\nu_x/dI_x$ is given by the (2 0 0 0) component of the DA vector $\mu(1)$ multiplied by a factor of two, which is due to the choice of normal-form basis vectors in COSY with magnitude $\sqrt{2I}$. Similarily, the quadratic tune shift with amplitude can be obtained from the next-order components of the normal-form tune vector by multiplication with a factor 4.

Linear tune shifts with amplitude (or rather action) for various conditions are listed in Table 2. The table confirms that the fringe fields of the matching quadrupoles are the dominant nonlinear effect. Without these fringes the linear tune shifts are much reduced and the contribution from the sextupoles becomes dominant. This is also reflected by the size of the tune footprints shown in Fig. 10. The so-called bare lattice in the last column includes the full kinematic correction. Its effect is negligible compared with sextupoles and fringe fields.

In an attempt to further optimise the dynamic aperture, we scanned the tunes by $\pm 0.1$ units around the original working points of 0.623 and 0.316. Figures 11 and 12 show results of 9th order map tracking with sextupoles and fringe fields in straights and arcs, *i.e.*, not including the fringes in the matching quadrupoles.

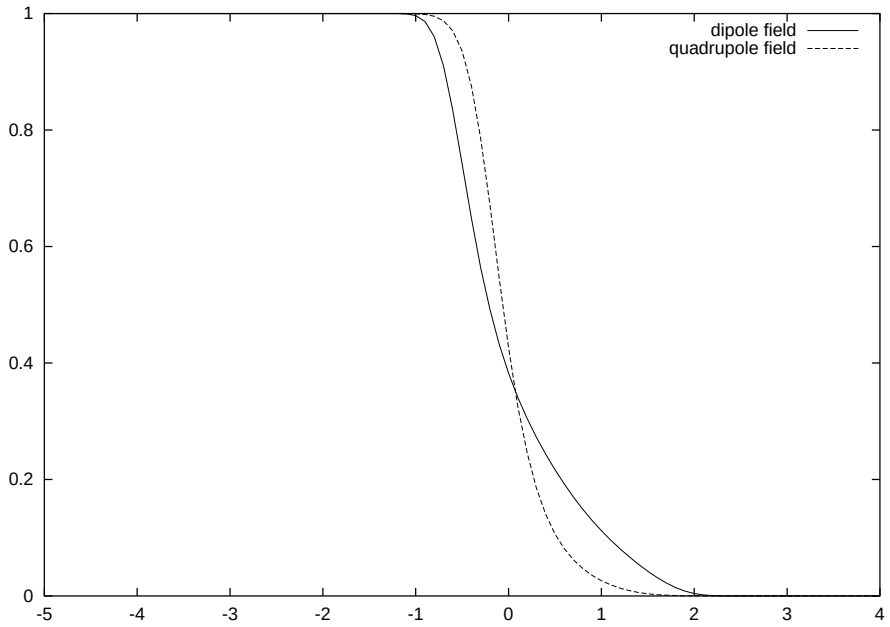


Figure 2: The fall-off of dipole and quadrupole fields assumed in the COSY fringe calulations, as a function of the longitudinal distance from the magnet edge in units of the full magnet aperture. The fall-off is described by an Enge function $F(z)$, as in Eq. (1), with coefficients inferred from PEP magnets [5].

We observe a rather strong dependence on the tunes, in particular a reduction of the dynamic aperture near the 3rd integer resonance. For the nominal tunes (the far-right picture in the second row) the dynamic aperture is about maximum.

Octupole correctors can reduce the detuning with amplitude and, thereby, possibly increase the dynamic aperture. An octupole of strength $k_o$ in units of $\mathrm{m}^{-4}$ as defined by MAD, corresponds to a pole-tip field of $B_T = k_o a_o^3/6$, where $a_o$ is the octupole bore radius. In first order perturbation theory, an octupole of strength $k_o$ and length $l_o$ introduces the following nonlinear Hamlitonan:

$$H = \frac{k_o l_o}{24}\left[x^4 - 6x^2y^2 + y^4\right] \tag{2}$$

and the amplitude-dependent tune shifts

$$\Delta\nu_x = \frac{1}{2\pi}\frac{k_o l_o}{8}\left[\beta_x^2 I_x - 2\beta_x\beta_y I_y\right] \tag{3}$$

$$\Delta\nu_y = \frac{1}{2\pi}\frac{k_o l_o}{8}\left[\beta_y^2 I_y - 2\beta_x\beta_y I_y\right] \tag{4}$$

For the simple example of a single octupole, we verified that the DA vector components of the amplitude-dependent tunes obtained from the COSY normal-form analysis are consistent with the coefficients in Eqs. (3) and (4).

Three octupoles are sufficient to cancel the three linear tune shifts with amplitude. So, we positioned the three octupoles in the dispersion-three return straight, at a defocusing quadrupole, the next focusing quadrupole, and at the center of the intermediate drift space, respectively. This arrangement does not generate any higher order dispersive components, and, by putting the octupoles at places with different ratios $\beta_x/\beta_y$ we avoid degeneracy. Using COSY, we chose the octupole strengths such that the linear tune shift with amplitude was exactly canceled. The corresponding phase space is shown in Fig. 13. The horizontal dynamic aperture is slightly improved, but the performance in the vertical plane deteriorates. The nonlinearities may also be corrected by sextupoles, instead of octupoles. Using three sextupoles, we tried to minimise either the linear tune shifts, or, alternatively, the norm of the third order map. These attempt were not successful. The dynamic aperture shrank to almost zero in both transverse planes.

An important issue is the dynamic aperture for off-energy particles. We recall that the energy acceptance of the ring should be $\pm 3\%$. Figures 14 and 15 depict the horizontal and vertical phase space, calculated by MAD, for seven different energy offsets varying from $-3$ to $+3\%$. Especially for large energy offsets, the dynamic aperture decreases strongly. It is essentially zero at an offset of $-3\%$. The blurry character of most trajectories indicates chaotic (potentially unstable) behavior. Figures 16 and 17 depict the equivalent phase space images, obtained from tracking through a 7th order map in three degrees of freedom, using COSY. The additional phase space distortions induced by fringe fields in arcs and straight sections, if any, can be seen in Figs. 18 and 19. Finally, Fig. 20 shows the horizontal phase space at the two extreme values of $+3\%$ and $-3\%$ for different values of the horizontal tune, which is varied between 0.6229 and 0.7429.

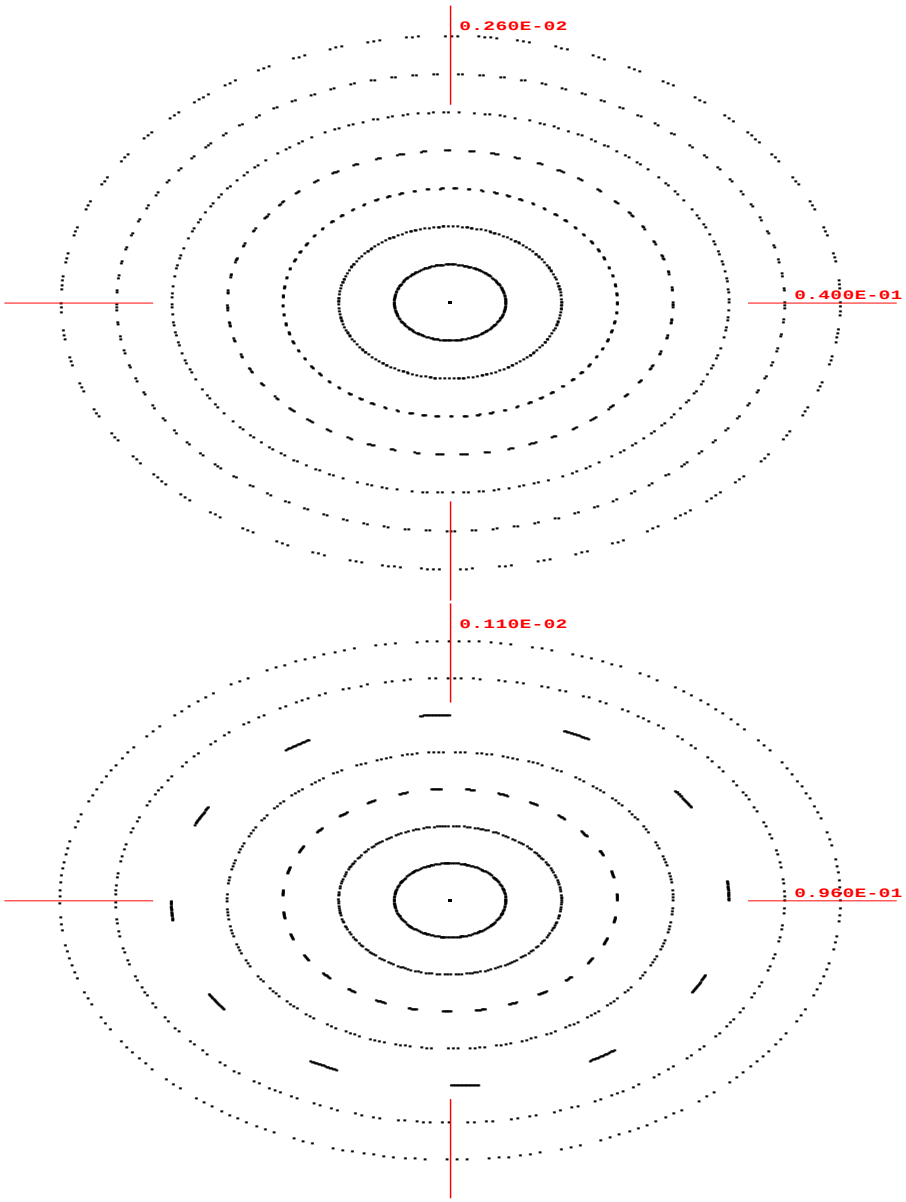


Figure 3: Horizontal (top) and vertical phase space (bottom), obtained by 9th order tracking through the full muon storage ring, without quadrupole fringe fields and without chromatic-correction sextupoles. Beta functions at the observation point are $\beta_x = 15$ m, $\beta_y = 87$ m. Particles are launched in steps of about $0.5\sigma$, and the plot range extends over about $\pm 4\sigma$. The energy offset is zero.

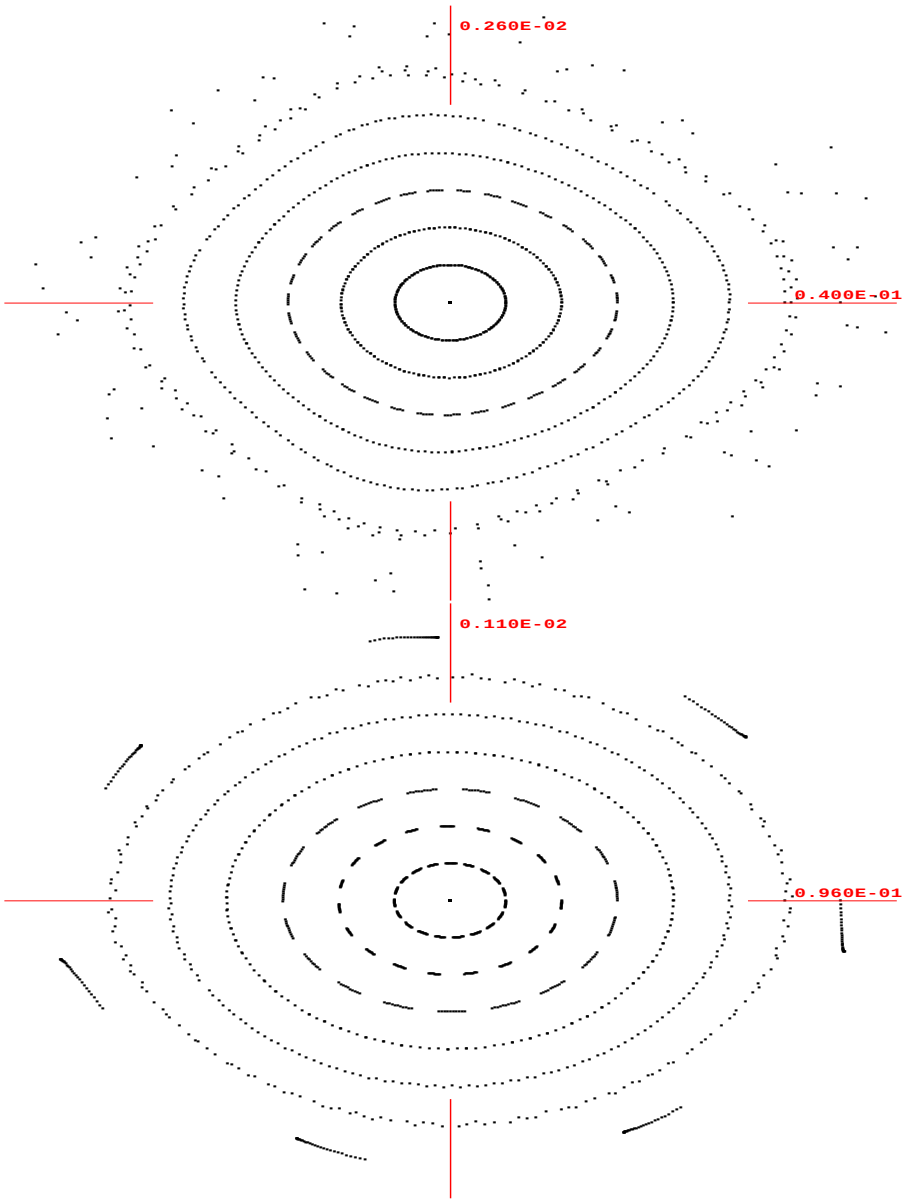


Figure 4: Horizontal (top) and vertical phase space (bottom), obtained by 9th order tracking with chromatic-correction sextupoles, but without quadrupole fringe fields. Beta functions at the observation point are $\beta_x = 15$ m, $\beta_y = 87$ m. Particles are launched in steps of about $0.5\sigma$, and the plot range extends over about $\pm 4\sigma$. The energy offset is zero.

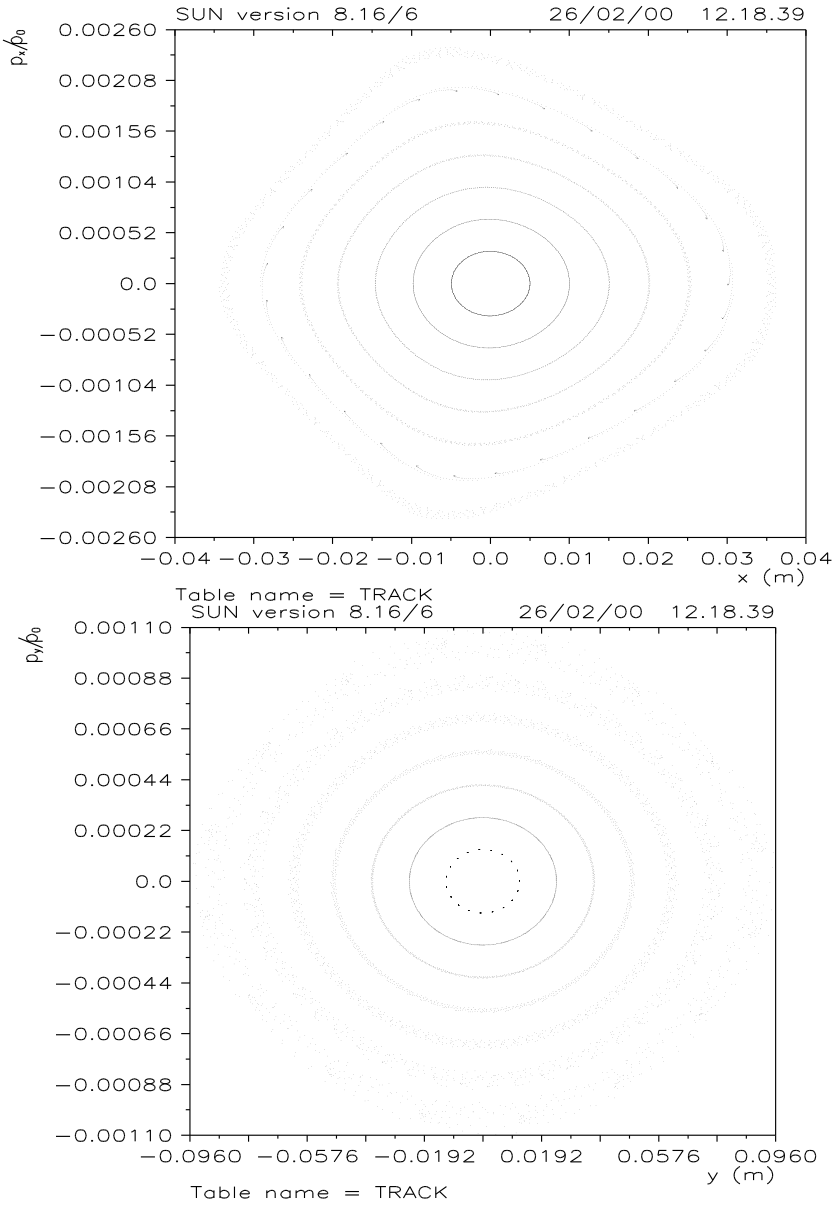


Figure 5: Horizontal (top) and vertical phase space (bottom), obtained by MAD tracking with chromatic-correction sextupoles, but without quadrupole fringe fields. Beta functions at the observation point are $\beta_x = 15$ m, $\beta_y = 87$ m. Particles are launched in steps of about $0.5\sigma$, and the plot range extends over about $\pm 4\sigma$. The energy offset is zero.

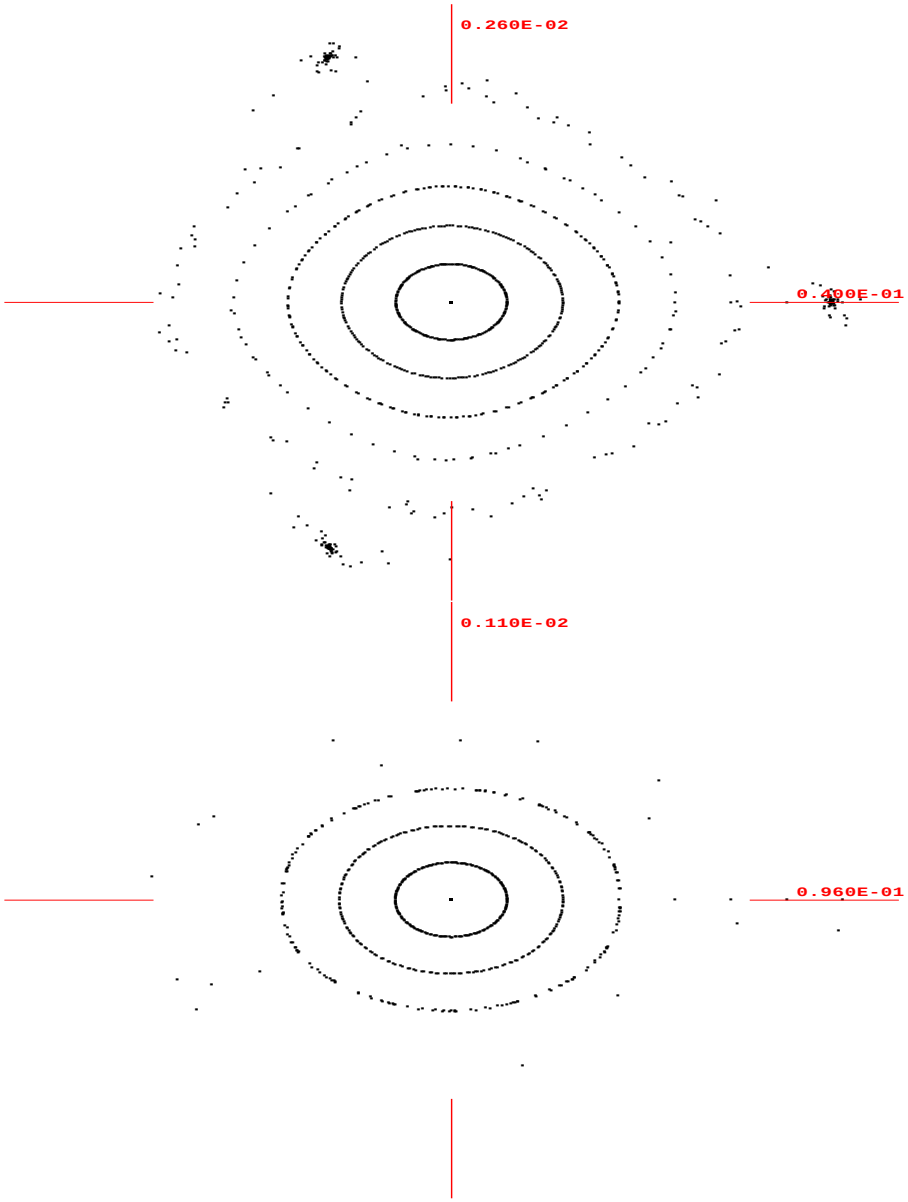


Figure 6: Horizontal (top) and vertical phase space (bottom), obtained by 9th order tracking through the full muon storage ring, including chromatic-correction sextupoles, and quadrupole fringe fields. Beta functions at the observation point are $\beta_x = 15$ m, $\beta_y = 87$ m. Particles are launched in steps of about $0.5\sigma$, and the plot range extends over about $\pm 4\sigma$. The energy offset is zero.

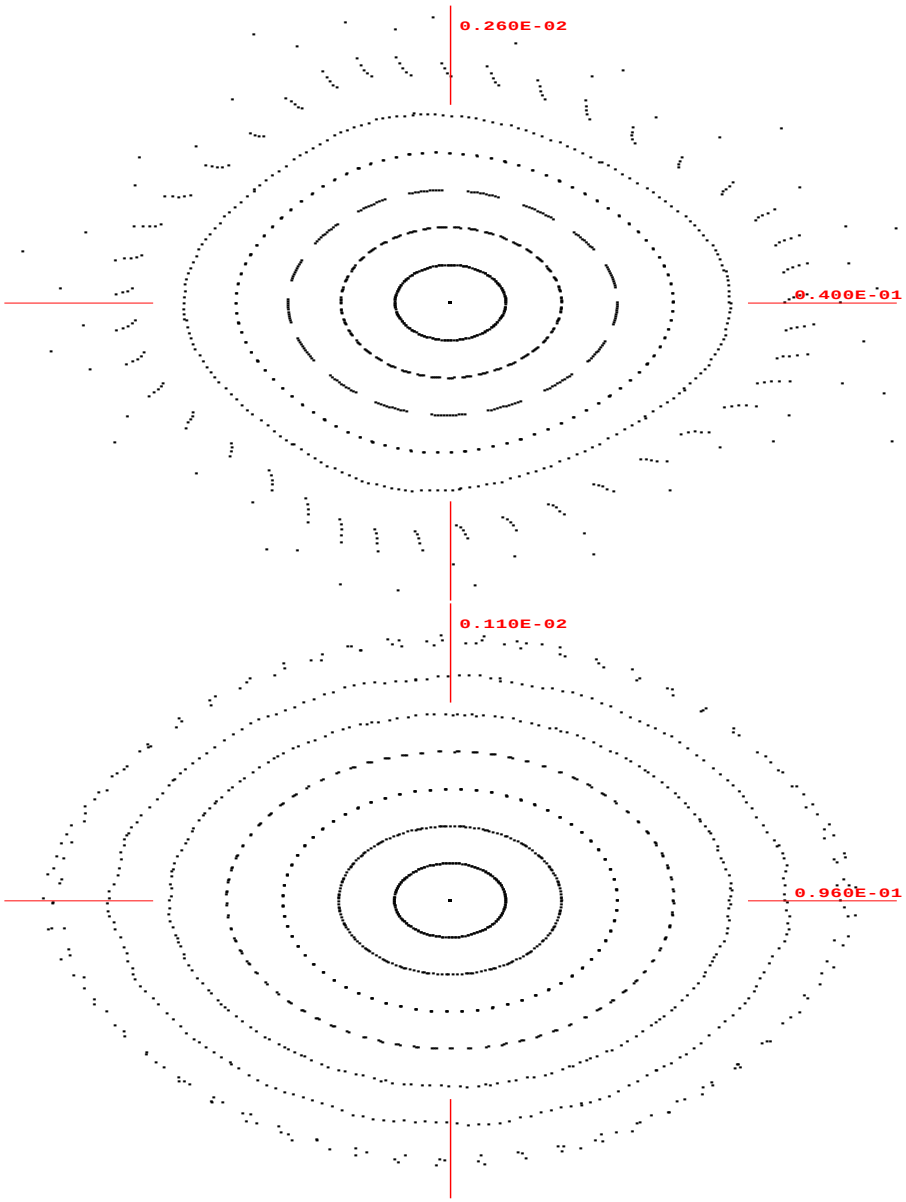


Figure 7: Horizontal (top) and vertical phase space (bottom), obtained by 9th order tracking through the full muon storage ring with chromatic-correction sextupoles, and with all quadrupole fringe fields, except those in the matching section, and Beta functions at the observation point are $\beta_x = 15$ m, $\beta_y = 87$ m. Particles are launched in steps of about $0.5\sigma$, and the plot range extends over about $\pm 4\sigma$. The energy offset is zero.

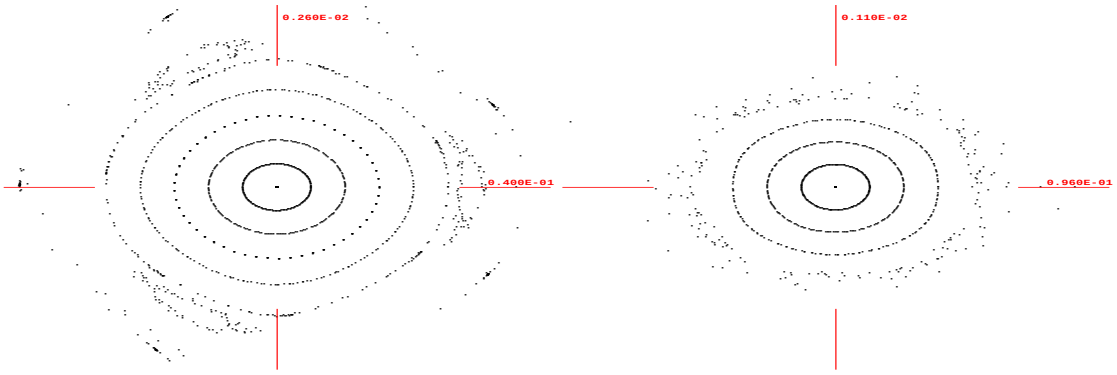


Figure 8: Horizontal (left) and vertical phase space (right), obtained by 11th order tracking through the full muon storage ring, including chromatic-correction sextupoles, and quadrupole fringe fields. Beta functions at the observation point are $\beta_x = 15$ m, $\beta_y = 87$ m. Particles are launched in steps of about $0.5\sigma$, and the plot range extends over about $\pm 4\sigma$. The energy offset is zero.

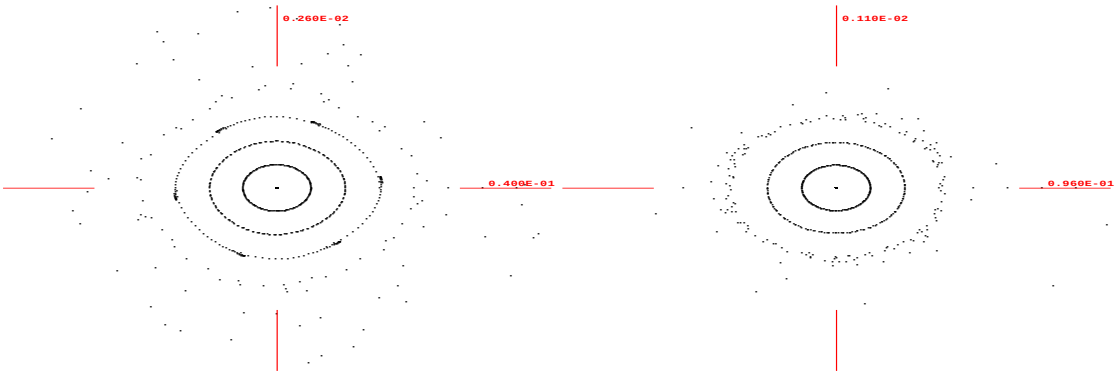


Figure 9: Horizontal (left) and vertical phase space (right), obtained by *7th order* tracking through the full muon storage ring, *including chromatic-correction sextupoles, and quadrupole fringe fields.* Beta functions at the observation point are $\beta_x = 15$ m, $\beta_y = 87$ m. Particles are launched in steps of about $0.5\sigma$, and the plot range extends over about $\pm 4\sigma$. The energy offset is zero.

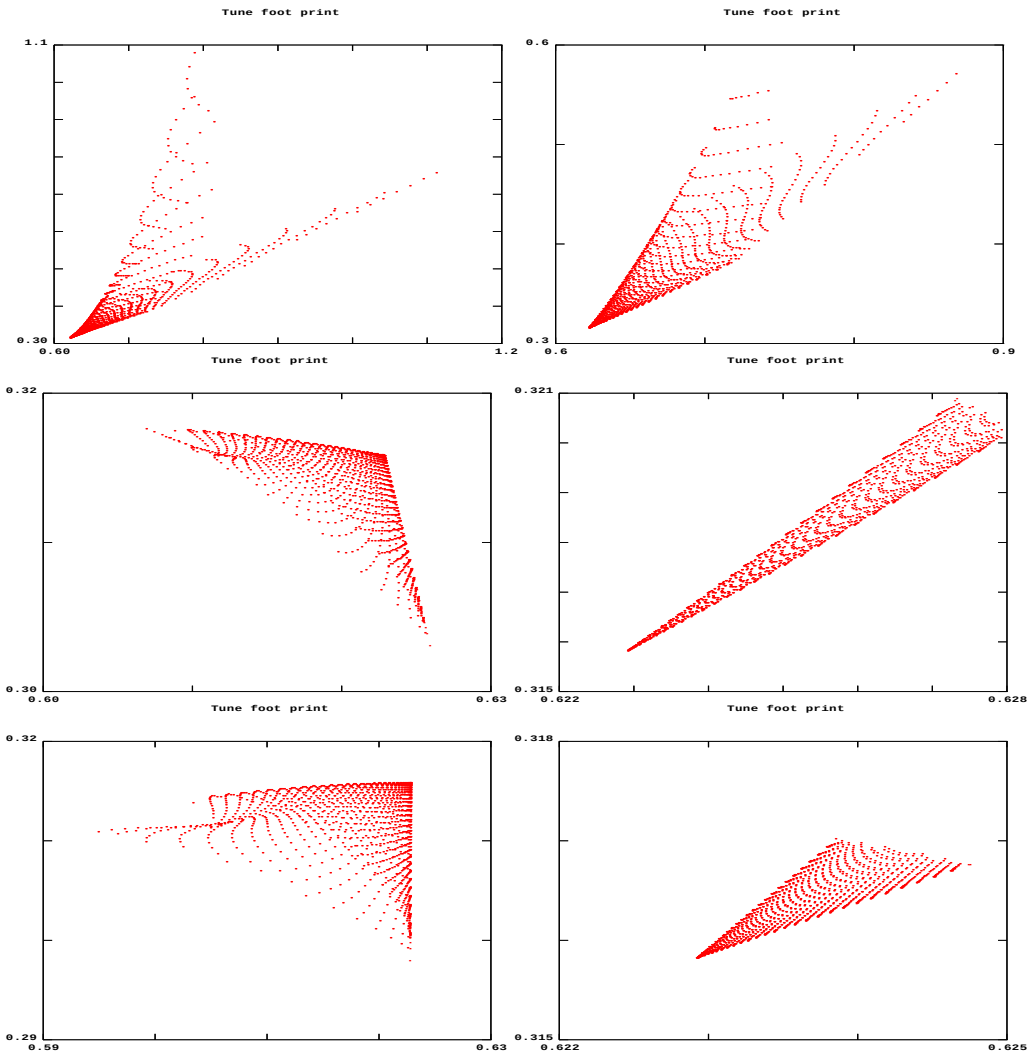


Figure 10: Tune foot print for horizontal and vertical starting amplitudes up to $3\sigma$, calculated from 5th order normal form. Top left: full lattice including sextupoles and fringes; top right: only fringes; center left: full lattice including sextupoles and all fringes except those in the matching quadrupoles; center right: fringes without matching quadrupoles and no sextupoles; bottom left: only sextupoles; bottom right: bare lattice.

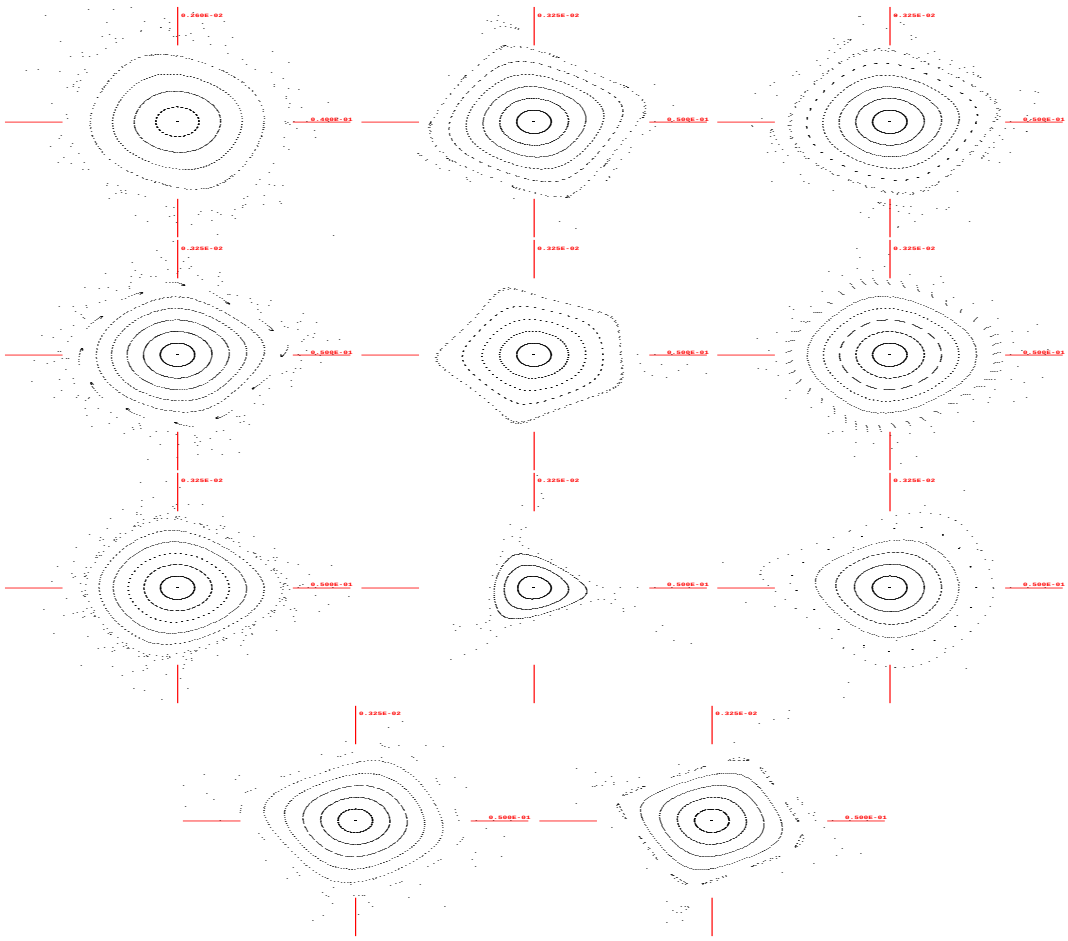

Figure 11: Horizontal phase space with 9th order map including sextupoles and fringe fields (except those in matching quadrupoles) for several values of the horizontal tune, varying from 0.523 (top left) to 0.723 (bottom right) in steps of 0.02. Each plot extends over $\pm 5\ \sigma$.

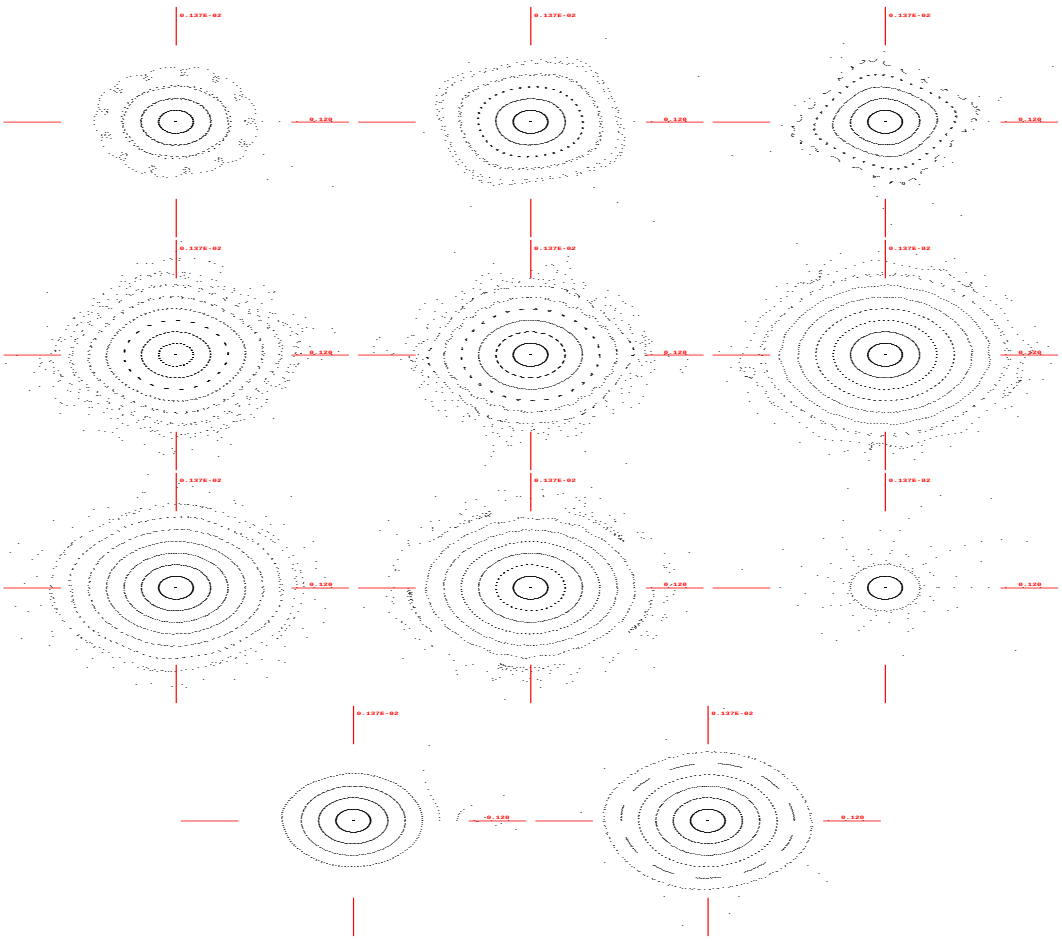

Figure 12: Vertical phase space with 9th order map including sextupoles and fringe fields (except those in matching quadrupoles) for several values of the vertical tune, varying from 0.216 (top left) to 0.416 (bottom right) in steps of 0.02. Each plot extends over $\pm 5\ \sigma$.

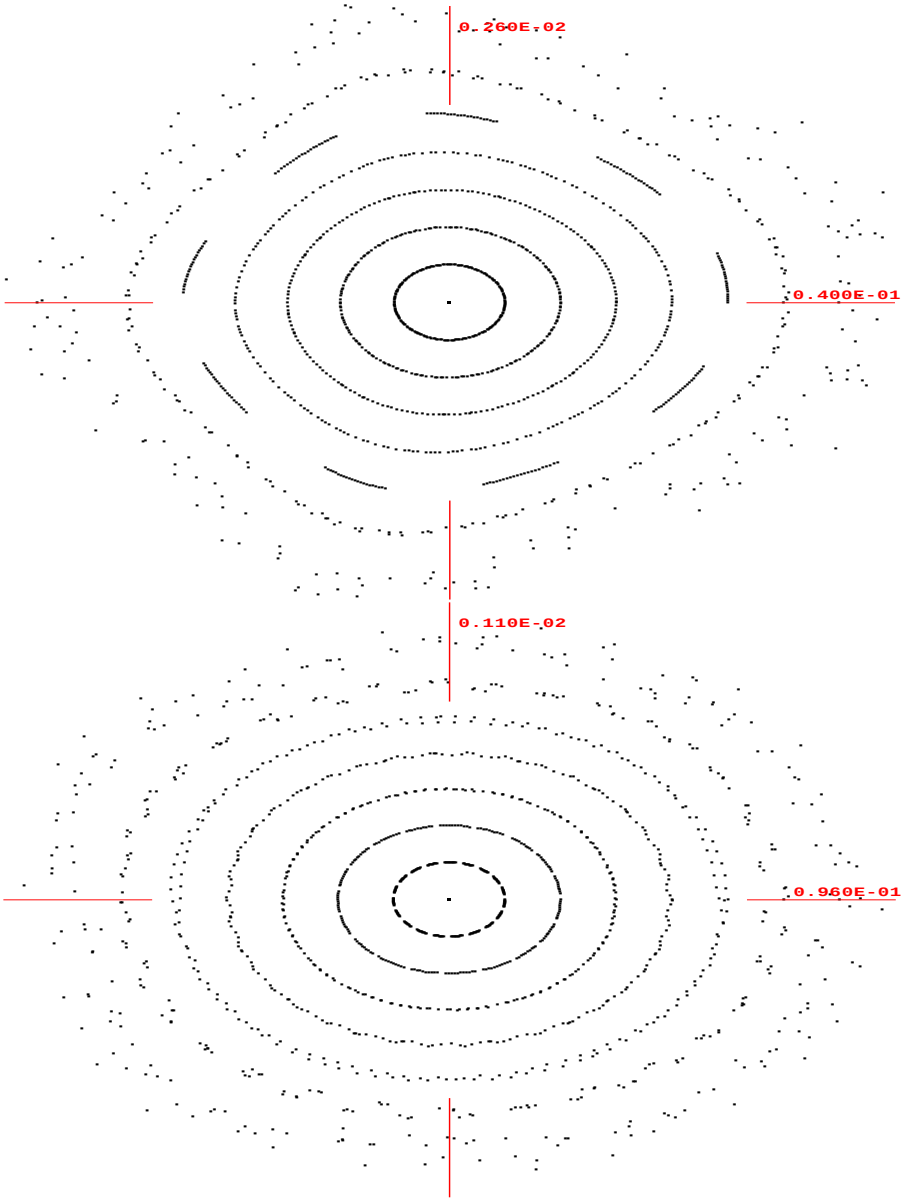


Figure 13: Horizontal (left) and vertical phase space (right), obtained by 9th order tracking through the full muon storage ring, including a set of *three octupole correctors* which exactly zero the linear tune shift with amplitude, as well as the chromatic-correction sextupoles, and all quadrupole fringe fields, except those in the matching section. Beta functions at the observation point are $\beta_x = 15$ m, $\beta_y = 87$ m. Particles are launched in steps of about $0.5\sigma$, and the plot range extends over about $\pm 4\sigma$. The energy offset is zero.

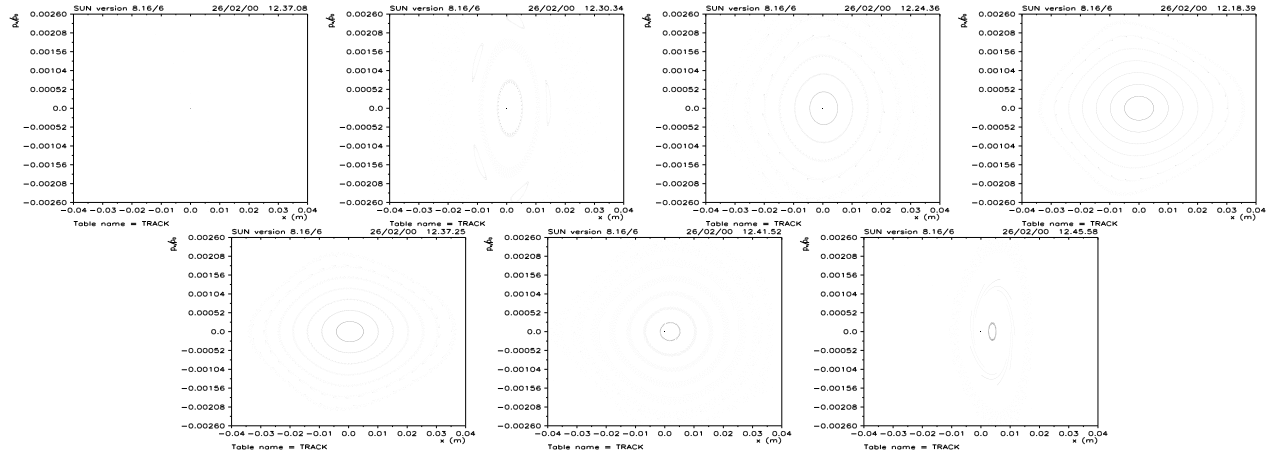


Figure 14: Horizontal phase space for different energy offsets, ranging from $-3\%$ to $+3\%$ in steps of 1%, as calculated by MAD. Fringe fields are not included. Each plot extends over $\pm 4\ \sigma$. Every turn is displayed.

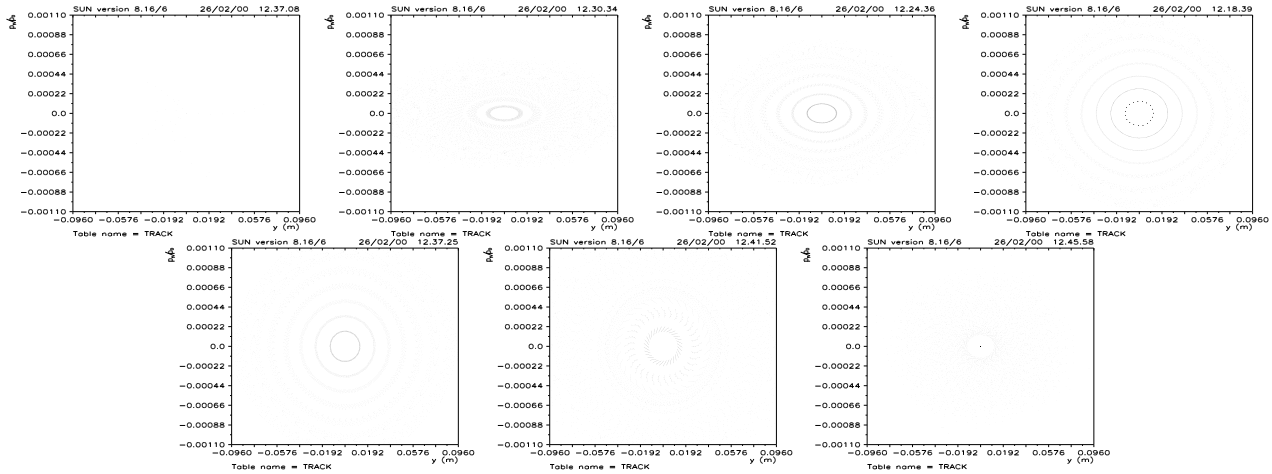


Figure 15: Vertical phase space for different energy offsets, ranging from $-3\%$ to $+3\%$ in steps of 1%, as calculated by MAD. Fringe fields are not included. Each plot extends over $\pm 4\ \sigma$. Every turn is displayed.

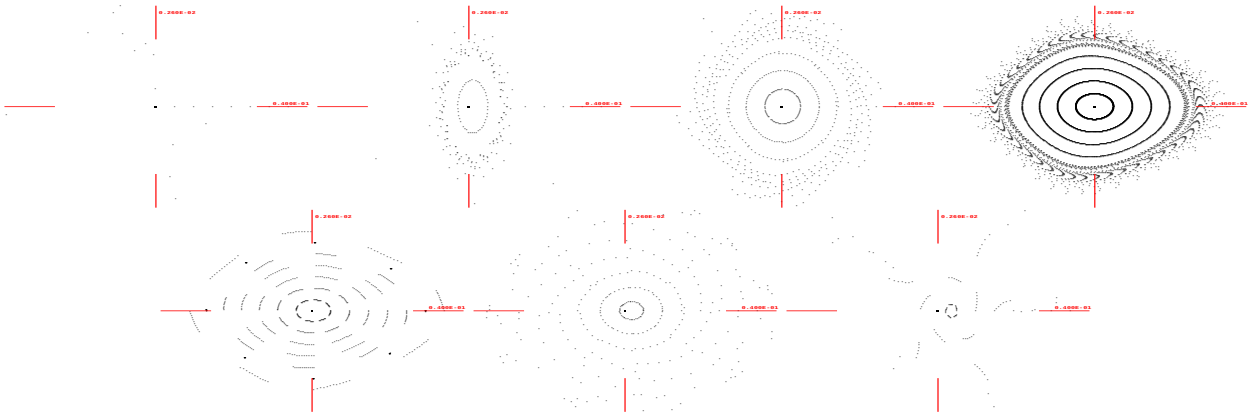

Figure 16: Horizontal phase space for different energy offsets, ranging from −3% to +3% in steps of 1%, as calculated by 7th order 3-dimensional tracking with COSY. Fringe fields are not included. Each plot extends over ±4 $\sigma$. Every turn is displayed.

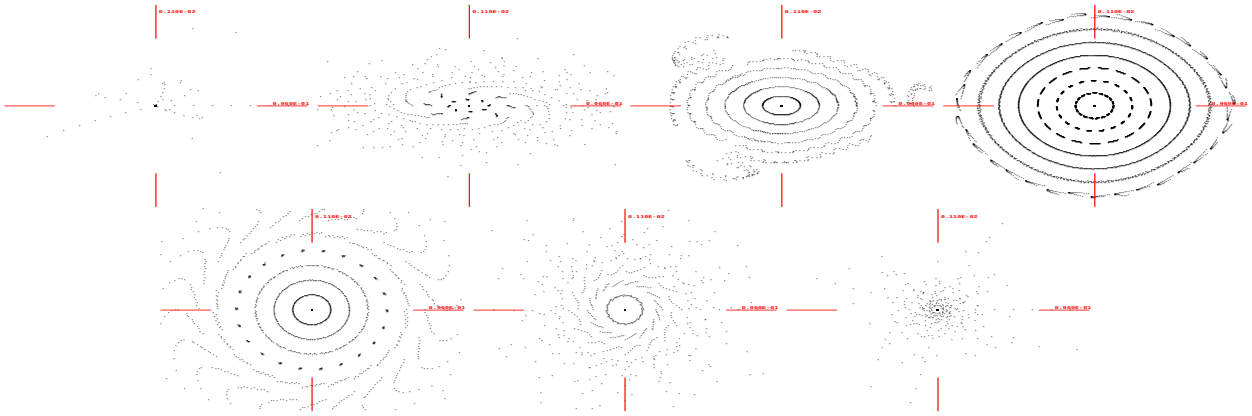

Figure 17: Vertical phase space for different energy offsets, ranging from −3% to +3% in steps of 1%, as calculated by 7th order 3-dimensional tracking with COSY. Fringe fields are not included. Each plot extends over ±4 $\sigma$. Every turn is displayed.

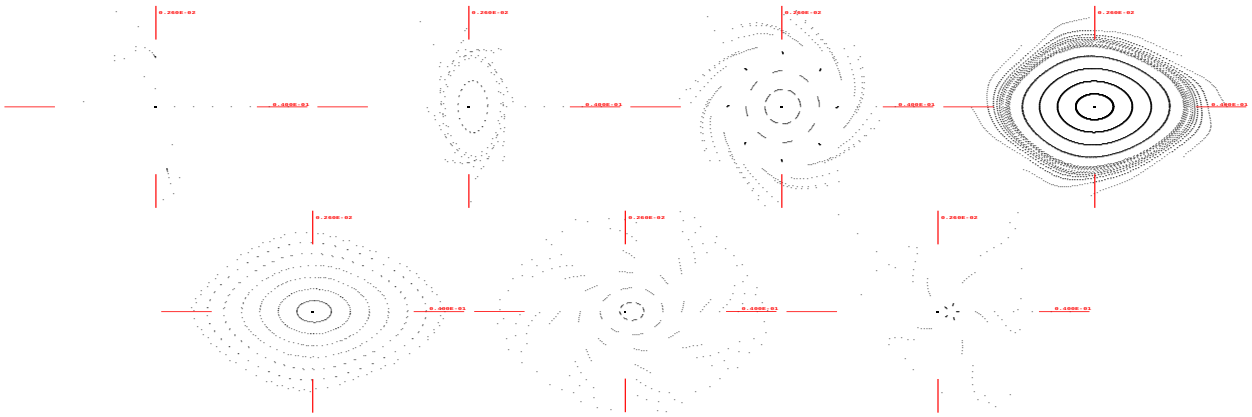

Figure 18: Horizontal phase space for different energy offsets, ranging from −3% to +3% in steps of 1%, as calculated by 7th order 3-dimensional tracking with COSY. Fringe fields are included except for those in the matching section. Each plot extends over ±4 $\sigma$. Every turn is displayed.

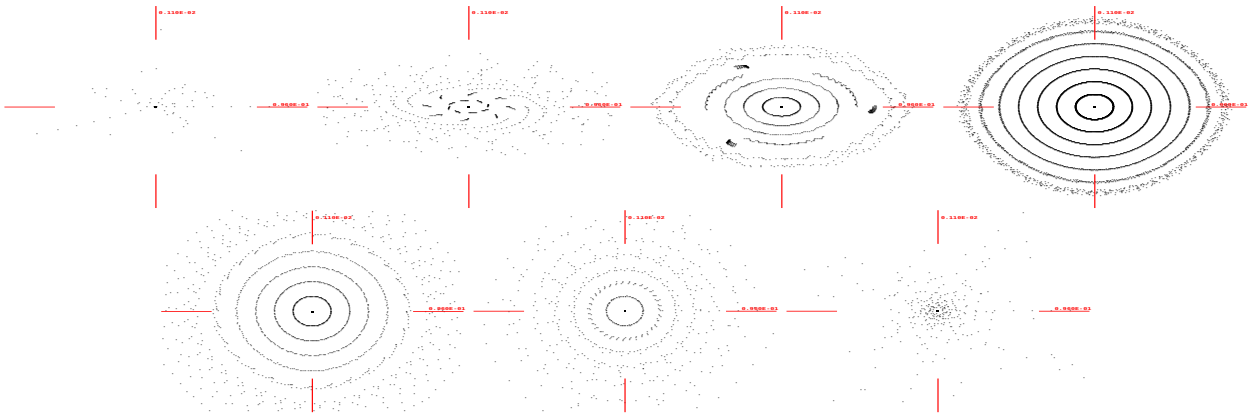

Figure 19: Vertical phase space for different energy offsets, ranging from −3% to +3% in steps of 1%, as calculated by 7th order 3-dimensional tracking with COSY. Fringe fields are included except for those in the matching section. Each plot extends over ±4 $\sigma$. Every turn is displayed.

Finally we look at the preservation of polarisation. The spin decoherence caused by different energies can be controlled via momentum compaction factor and rf voltage [9]. The spins can also decohere due to differences in the particle orbits. This question is addressed in Fig. 21, which displays the variation of the $n$-axis and the variation in spin tune for trajectories extending up to $\pm 3\sigma$ in transverse phase space. We estimate that the net depolarisation due to the dependence of spin motion on transverse coordinates is considerably less than 1%.

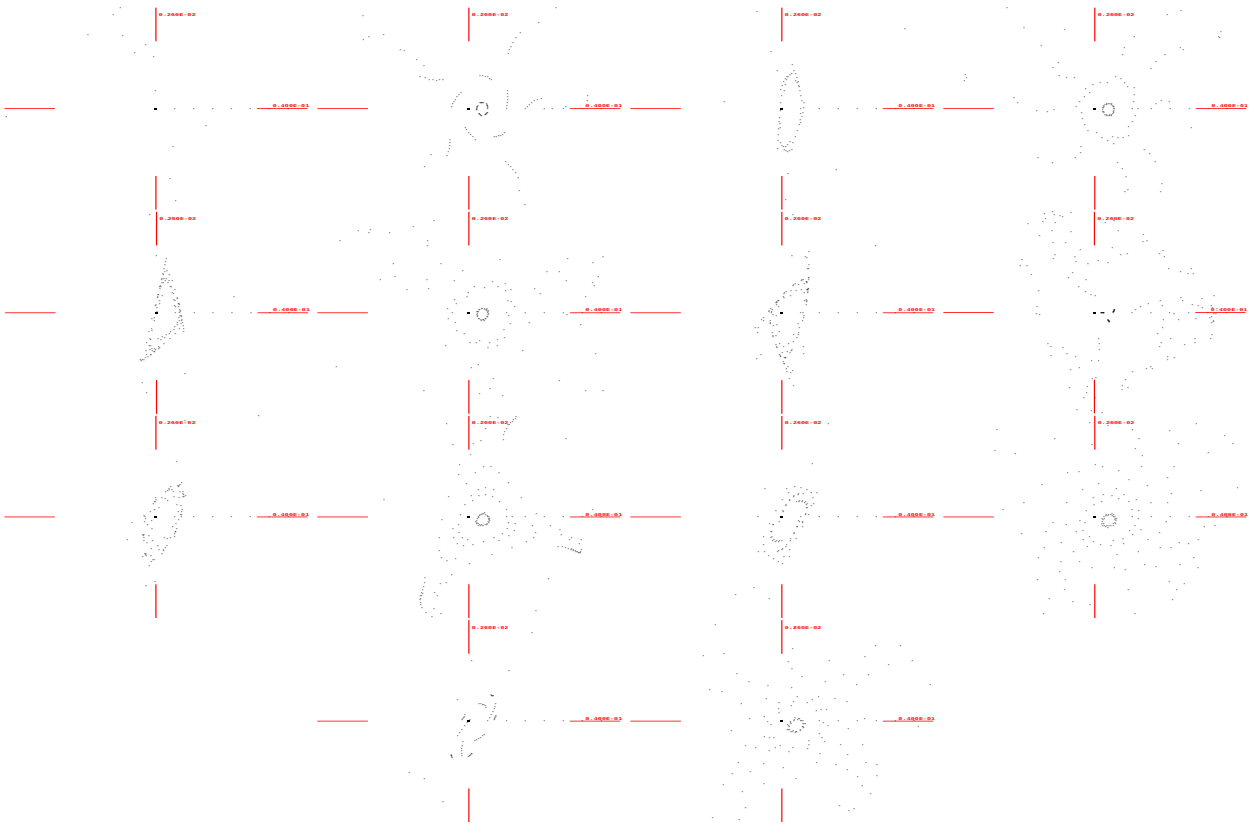

Figure 20: Horizontal phase space for energy offsets of ±3% (in alternating order). The fractional horizontal tune varies between 0.6229 (top left) and 0.7229 (bottom right) in steps of 0.02. The plots were obtained by 7th order 3-dimensional tracking with COSY. Fringe fields are not included. Each picture extends over ±4 $\sigma$, and every turn is displayed.

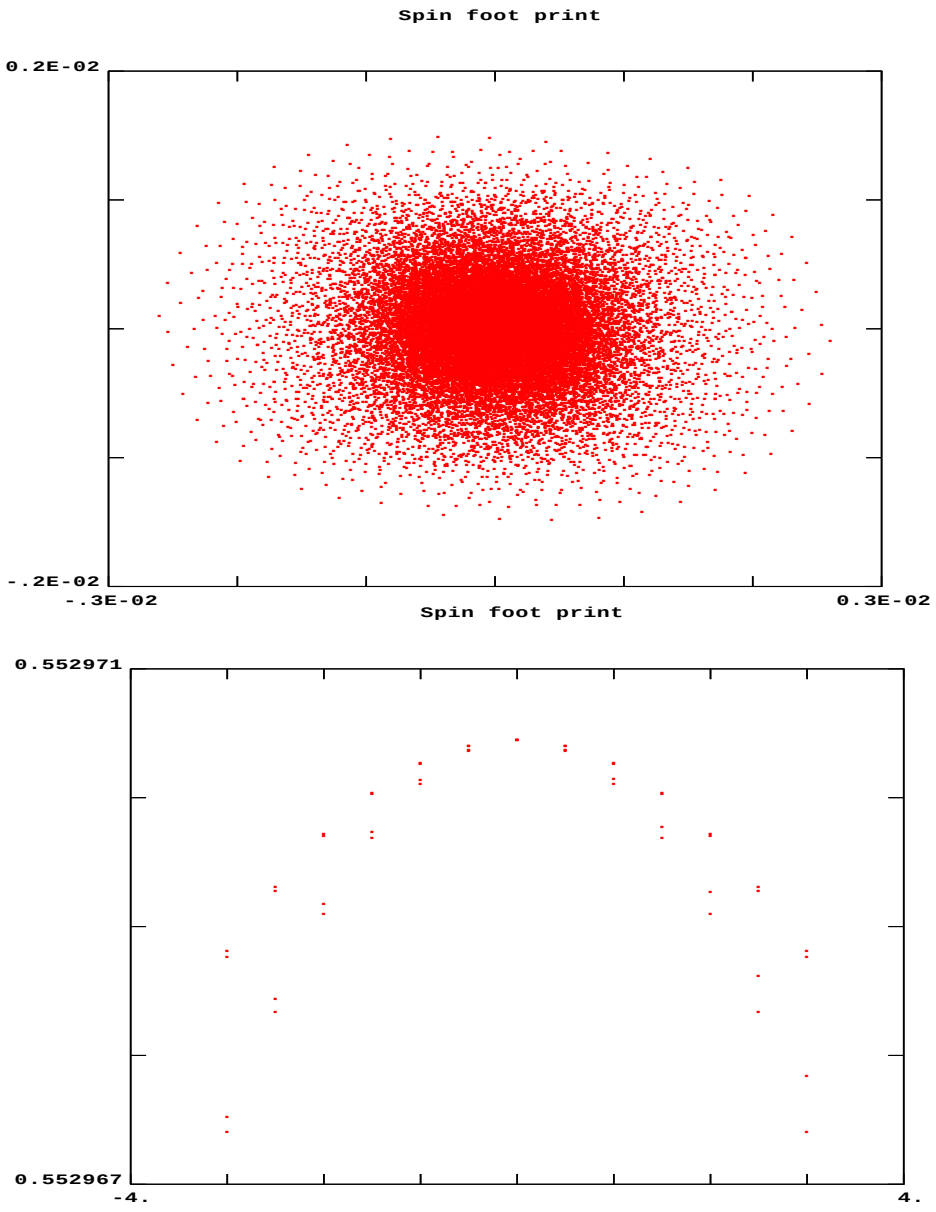


Figure 21: Spin footprints for the FNAL storage ring. Shown are the longitudinal and vertical components of the $n$-axis for transverse coordinates extending up to $\pm 3\sigma$ (left) and the spin tune [the rotation frequency around the $n$ axis] as a function of starting coordinates in units of $\sigma$ (right). The spin calculations were performed to 3rd order.

# 3 Tracking Results for the CERN Muon Storage Ring

Similar tracking studies were performed for the CERN muon storage ring. The optics is shown in Fig. 22 and parameters are listed in Table 3 [10].

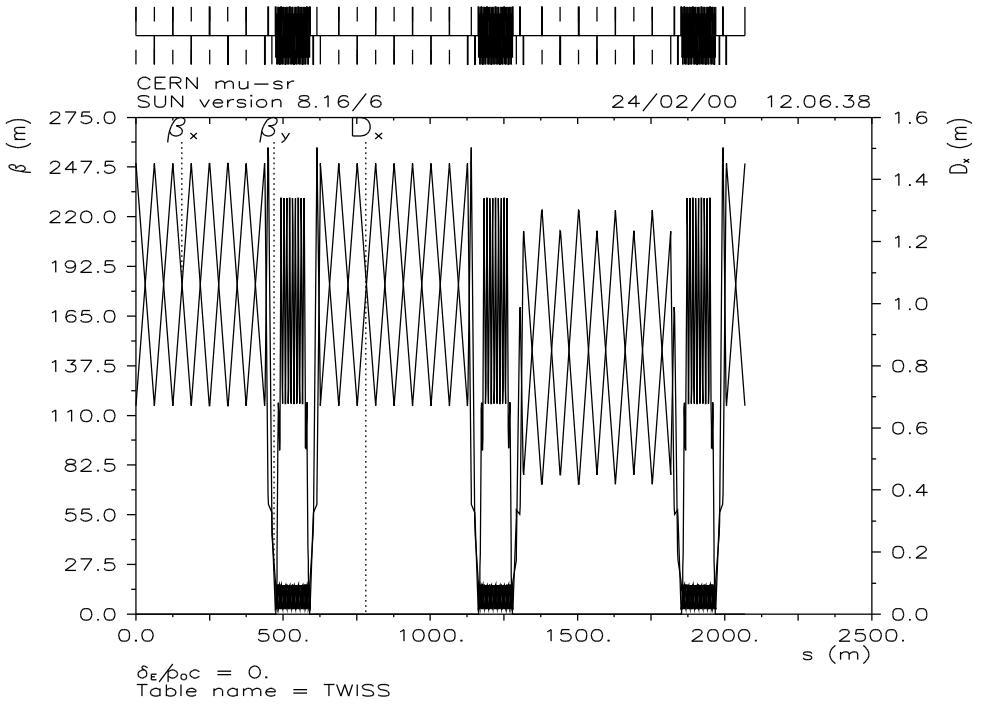


Figure 22: Optics of the CERN muon storage ring [10].

Figure 23 depicts the horizontal and vertical phase space obtained by tracking for 1000 turns (trajectories are displayed on every 5th turn) through a 9th order map, representing the CERN muon storage ring without fringe fields, but with chromatic-correction sextupoles. The dynamic aperture is $4\sigma$ or larger in both transverse planes.

Figure 24 shows that the fringe fields reduce the horizontal dynamic aperture to about 1 $\sigma$, whereas the dynamic aperture in the vertical plane is not compromised. Figure 25 shows that, in the same manner as for the FNAL design, the dynamic aperture can be almost fully recovered when we ignore the fringe fields in the matching sections.

A magnified view of the optics in the matching section of the CERN muon storage ring is shown in Fig. 26. The horizontally focusing quadrupole Q3M, located at $s = 451$ m, is almost two times stronger than its vertically focusing neighbor Q4M, near 432 m. Indeed, lengthening and weakening this quadrupole by a factor of two recovers the dynamic aperture. This is shown in Fig. 27. The optics was not rematched, which is the reason for the tilted phase space ellipse and the change in beta function.

The dynamic aperture for the full lattice, including all fringe fields, can be improved slightly, by moving the tune away from the 4th integer resonance, as is illustrated in Fig. 28. However, even with this optimisation the dynamic aperture is never larger than $1.5\sigma$. In the following we will set the horizontal tune to $\nu_x = 0.294$. The tune is changed artificially by inserting a rotation matrix (phase trombone) into the lattice.

Figure 29 shows the horizontal phase space, up to $4\sigma$, as obtained by tracking with an 11th order map. The result looks the same as for the 9th order calculation, Fig. 28 (top right). Hence, the small aperture is not an artifact of the map order.

Table 4 lists the linear tune shifts for the CERN muon storage ring calculated under various conditions. The linear tune shift including all fringes is smaller than that for the FNAL ring discussed earlier. Since at the same time the design emittance is also smaller, the dynamic aperture limitation is a little surprising. It must be caused either by resonance excitation and/or by the higher-order detuning with amplitude. Figure 30 depicts the tune footprints up to 5th order. Evidently, the higher-order tune shift with amplitude are

Table 3: Some parameters of the CERN muon storage ring, designed by E. Keil [10].

| | | |
|---|---|---|
| beam energy | $E$ | 50 GeV |
| normalized emittance | $\gamma\epsilon_{x,y}$ | 1.7 mm mrad |
| rms energy spread | $(\Delta p/p)_{\rm rms}$ | 0.5% |
| circumference | $C$ | 2068.8 m |
| betatron tunes | $\nu_{x,y}$ | 11.254, 12.287 |
| arc quad radius | $r_a$ | 3.1 cm |
| arc quad pole tip | $B_{T,a}$ | 3 T |
| arc quad length | $l_a$ | 0.5 m |
| arc dipole field | $B$ | 6 T |
| arc dipole length | $l$ | 2.9 m |
| straight-section quad radius | $r_p$ | 8.9 cm |
| straight-section quad pole tip | $B_{T,p}$ | 0.5 T |
| straight-section quad length | $l_p$ | 0.35 m |

Table 4: Linear tune shift for the CERN muon storage ring in various configurations. The bare lattice contains kinematic terms only.

| tune shift | $d\nu_x/dI_x$ | $d\nu_x/dI_y$ | $d\nu_y/dI_y$ |
|---|---|---|---|
| sexts. & fringes | 184 | -79 | 173 |
| sexts. & fringes w/o matching section | 104 | $-128$ | 163 |
| sexts. only | 44 | $-184$ | 107 |
| bare lattice | 5 | 3 | 5 |

huge when all fringe fields are present. Indeed, the second order tune shifts $d^2\nu_{x,y}/dI_{x,y}^2$ induced by the fringe fields are of the order of several $10^8$ per inverse square meter. Without fringes in the matching sections they are a factor 100 smaller.

As a side point we note that increasing the aperture of all magnets by a factor of two has only a marginal effect on detuning and dynamic aperture.

Again we attempt to increase the dynamic aperture with octupole correctors in the straight section. This time we tried to adjust the strengths of 4 octupoles such as to minimise the norm of the 4th order map. The resulting phase space, in Fig. 31, shows no sign of improvement.

Figures 32 and 33 depict the horizontal and vertical phase space for energy offsets varying between $-1.5\%$ and $+1.5\%$, as calculated by MAD, without any fringe fields. This simulation includes collimators representing magnet apertures, at which many of the tracked particles are lost. Figures 34 and 35 are the corresponding pictures from a 7th order tracking with COSY. Here the fringe fields are included, except for those in the matching sections, but collimators are not.

Figure 36 finally shows spin footprints for the CERN muon storage ring. Again, the depolarisation due to the dependence of spin motion on transverse phase space is weak.

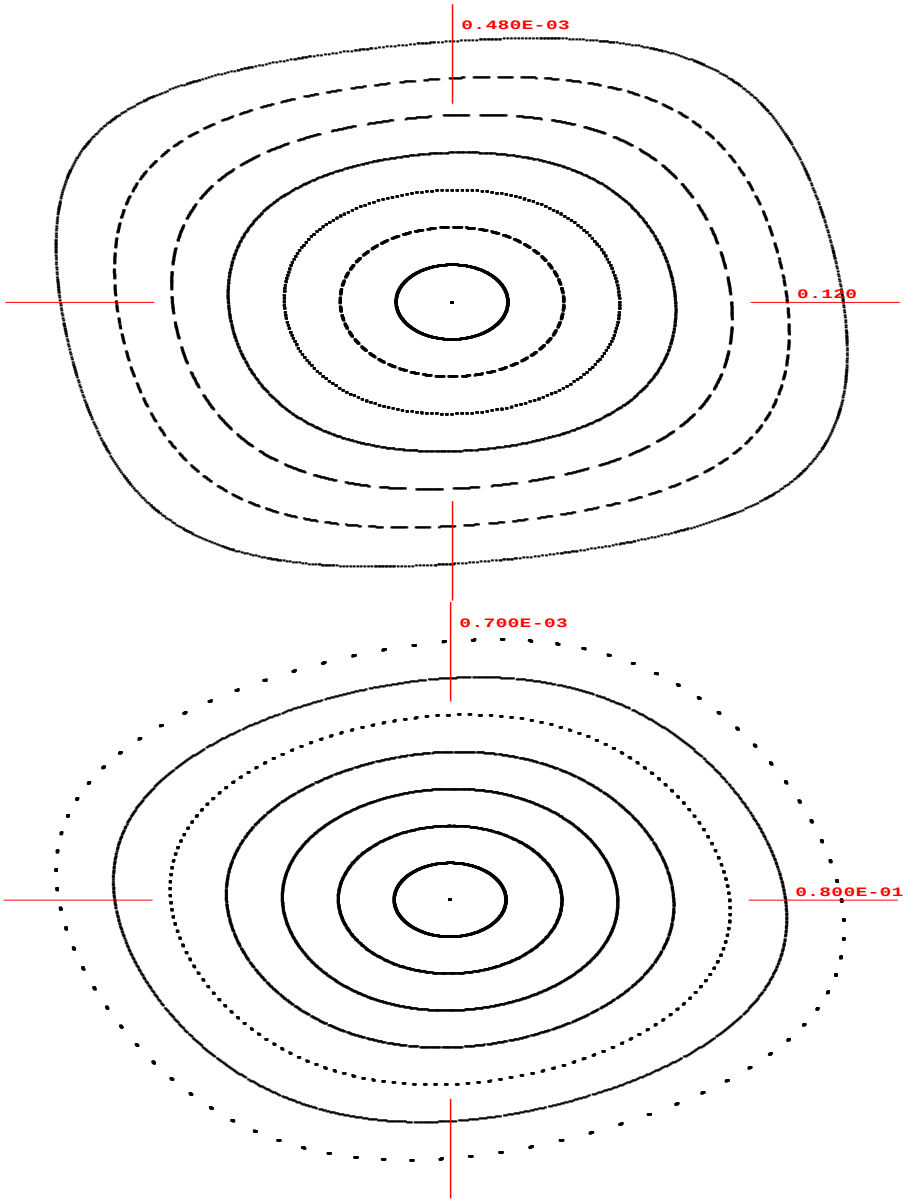


Figure 23: Horizontal (left) and vertical phase space (right), obtained by 9th order tracking through the CERN muon storage ring, with chromatic-correction sextupoles, but without fringe fields. Beta functions at the observation point are $\beta_x = 250$ m, $\beta_y = 115$ m. Particles are launched in steps of about $0.5\sigma$, and the plot range extends over about $\pm 4\sigma$. The energy offset is zero.

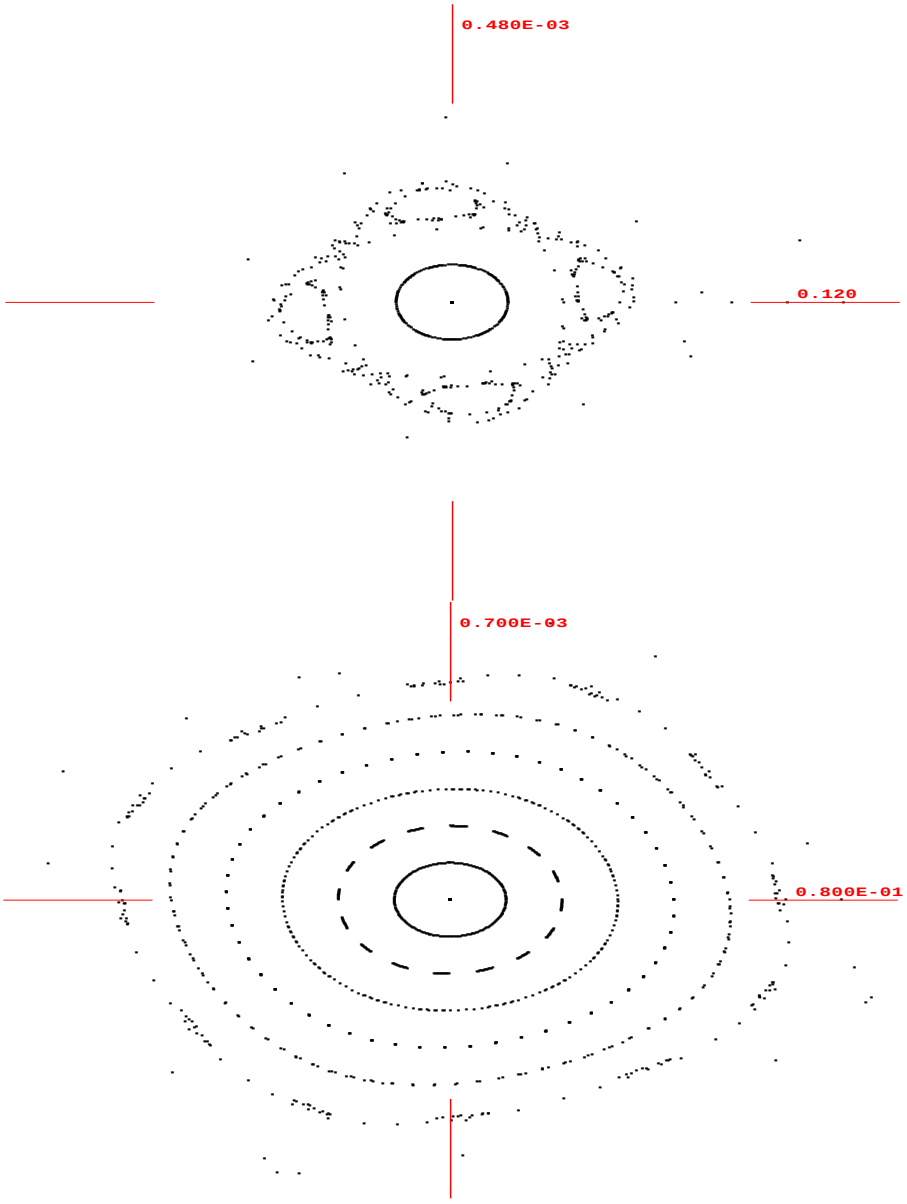


Figure 24: Horizontal (left) and vertical phase space (right), obtained by 9th order tracking through the CERN muon storage ring, including quadrupole fringe fields, and chromatic-correction sextupoles. Beta functions at the observation point are $\beta_x = 250$ m, $\beta_y = 115$ m. Particles are launched in steps of about $0.5\sigma$, and the plot range extends over about $\pm 4\sigma$. The energy offset is zero.

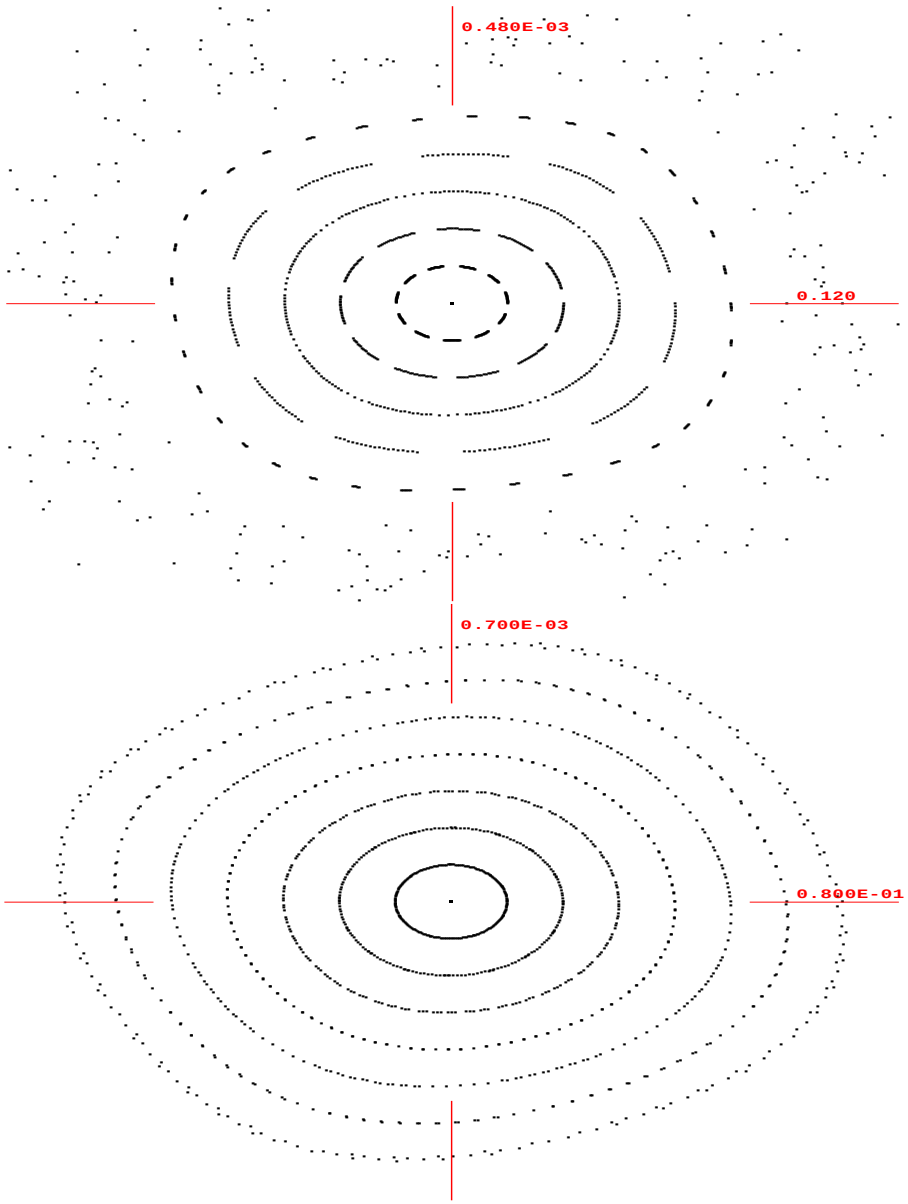


Figure 25: Horizontal (top) and vertical phase space (bottom), obtained by 9th order tracking through the CERN muon storage ring, including chromatic-correction sextupoles, and all quadrupole fringe fields except those in the matching sections. Beta functions at the observation point are $\beta_x = 250$ m, $\beta_y = 115$ m. Particles are launched in steps of about $0.5\sigma$, and the plot range extends over about $\pm 4\sigma$. The energy offset is zero.

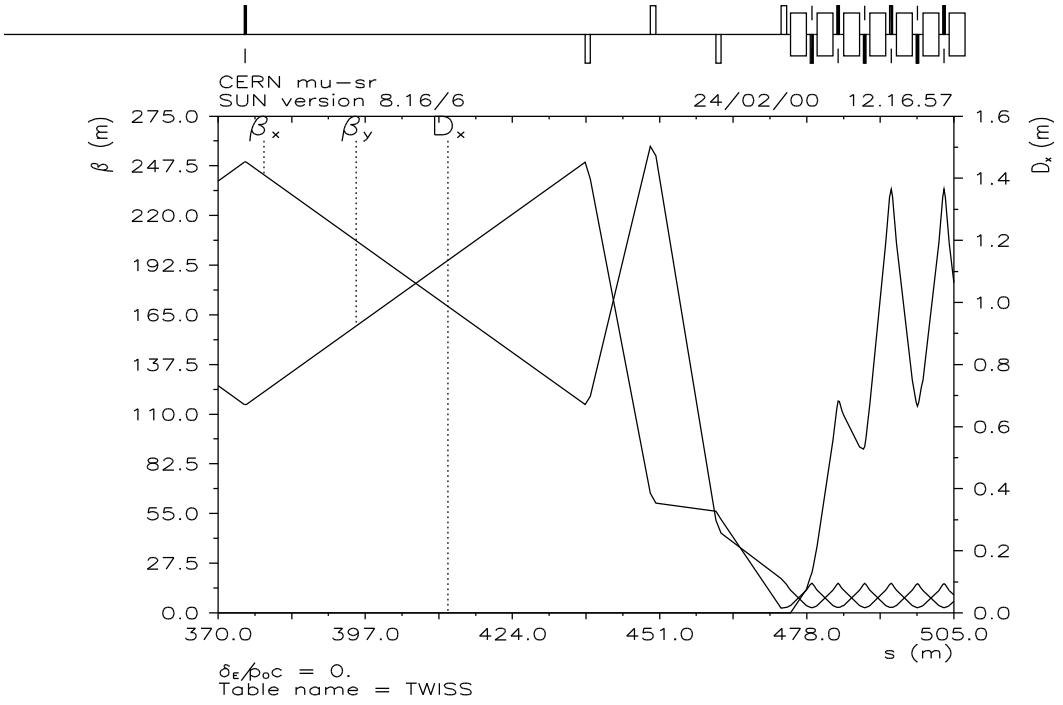


Figure 26: Optics of the matching section in the CERN muon storage ring [10].

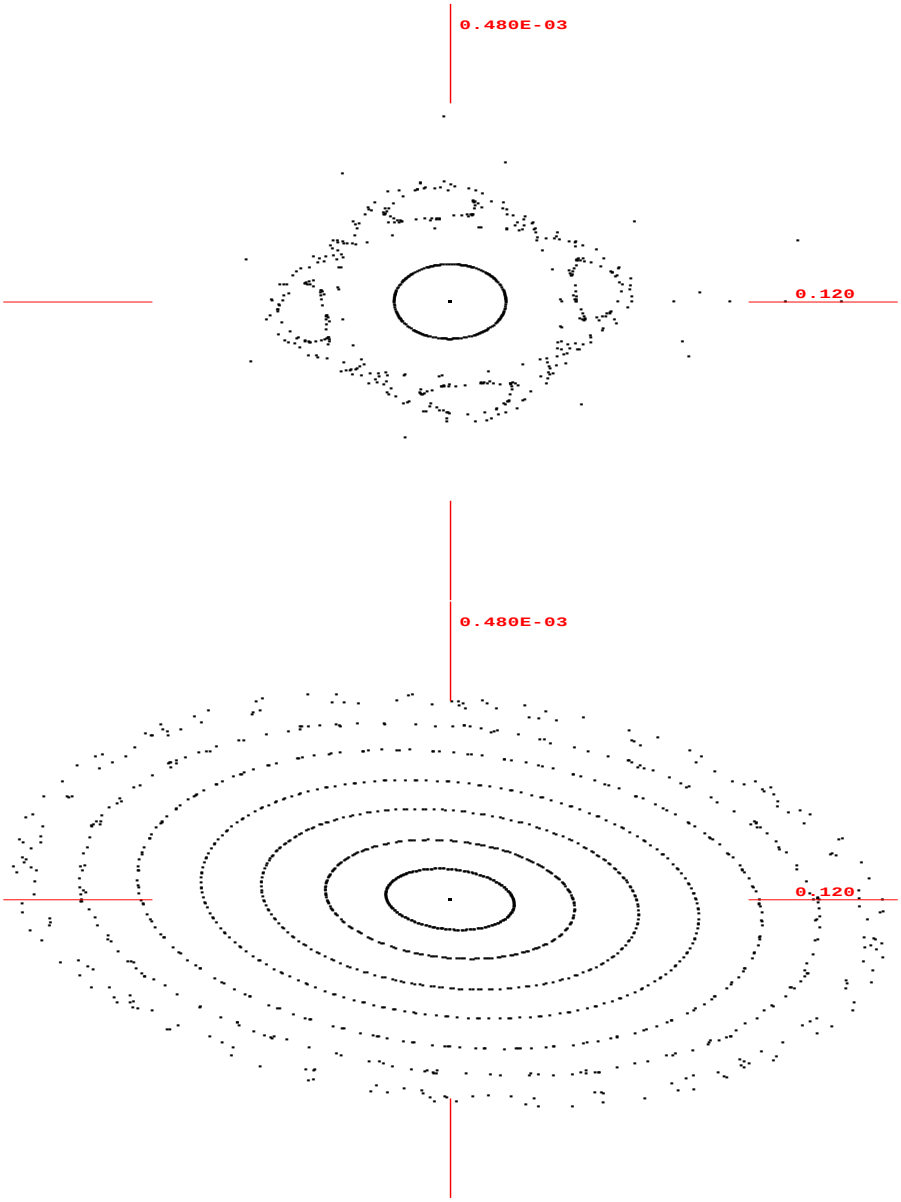


Figure 27: Horizontal phase space for two different lengths of Q3M, obtained by 9th order tracking through the CERN muon storage ring, including chromatic-correction sextupoles and quadrupole fringe fields. Top: original length of Q3M equal to 1 m; bottom: length 2 m, and correspondingly strength reduced by factor 2. The horizontal beta functions at the observation point are $\beta_x = 250$ m (top) and $\beta_x = 354$ m (bottom). Particles are launched in steps of about $0.5\sigma$, and the plot range extends over about $\pm 4\sigma$. The energy offset is zero.

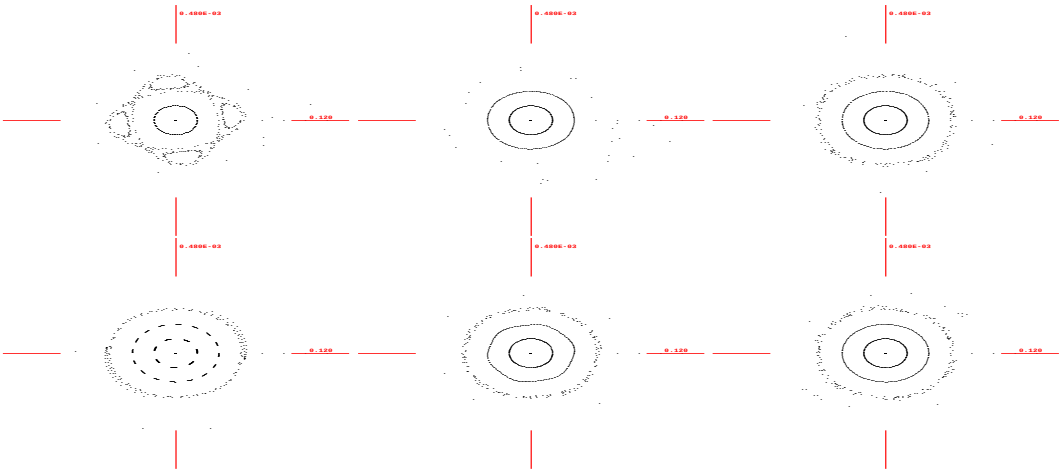

Figure 28: Horizontal phase space with 9th order map including sextupoles and fringe fields for several values of the horizontal tune, varying from 0.254 (nominal) to 0.354 in steps of 0.02. Each plot extends over $\pm 4\ \sigma$.

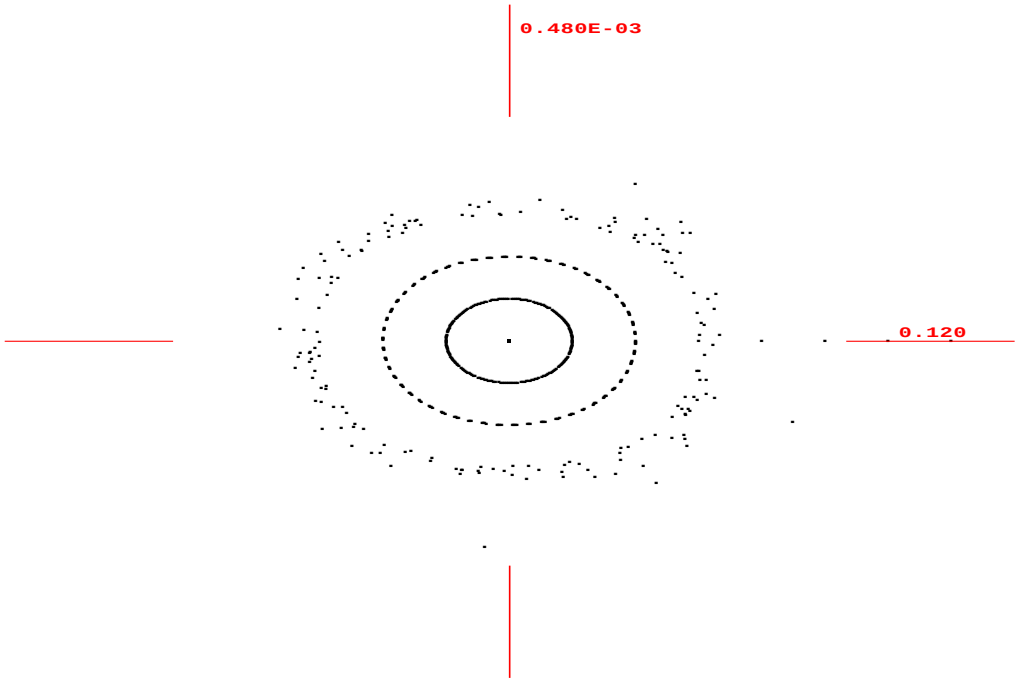


Figure 29: Horizontal phase space, obtained by 11th order tracking through the CERN muon storage ring, including chromatic-correction sextupoles, and all quadrupole fringe fields, with fractional tunes set to $\nu_x = 0.294$ and $\nu_y = 0.287$. Beta functions at the observation point are $\beta_x = 250$ m, $\beta_y = 115$ m. Particles are launched in steps of about $0.5\sigma$, and the plot range extends over about $\pm 4\sigma$. The energy offset is zero.

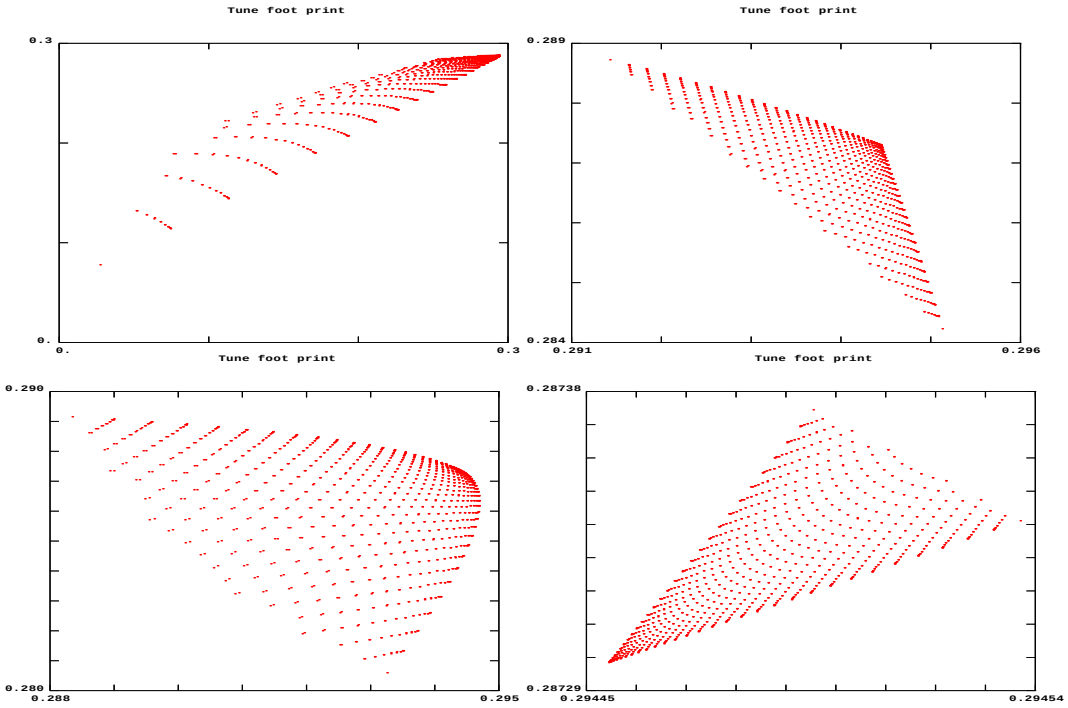


Figure 30: Tune footprint for the CERN muon storage ring with horizontal and vertical starting amplitudes up to $3\sigma$, calculated from 5th order normal form. Top left: full lattice including sextupoles and all fringes; top right: only sextupoles; bottom left: full lattice including sextupoles and all fringes except those in the matching quadrupoles; bottom right: bare lattice.

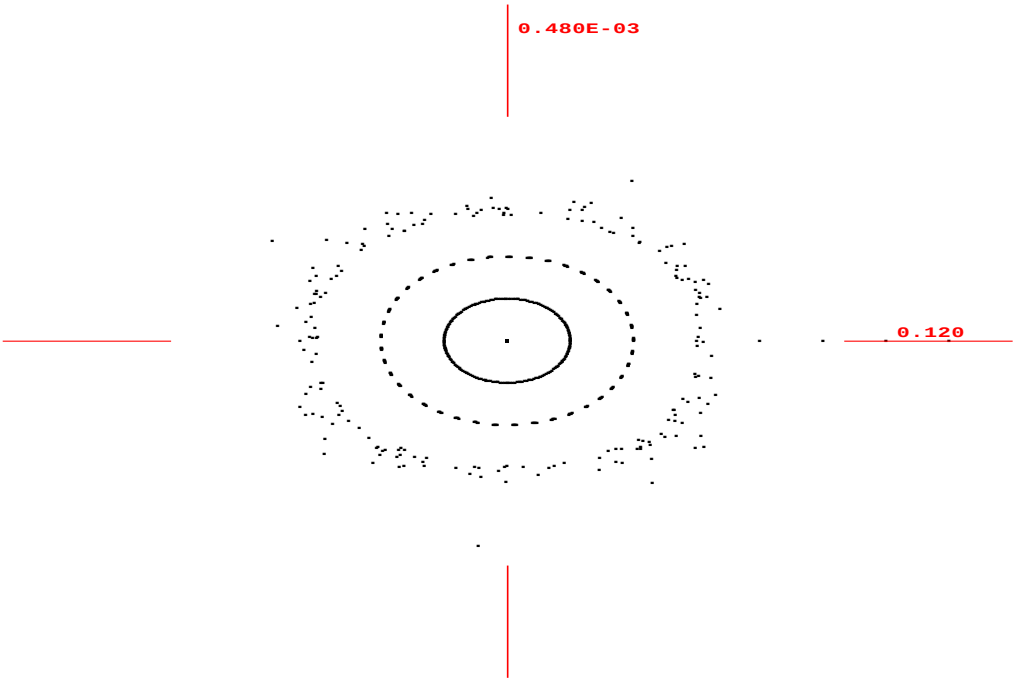


Figure 31: Horizontal phase space, obtained by 9th order tracking through the CERN muon storage ring, including a set of four octupole correctors which minimise the norm of the 4th order map, as well as chromatic-correction sextupoles, and all quadrupole fringe fields except those in the matching sections. Beta functions at the observation point are $\beta_x = 250$ m, $\beta_y = 115$ m. Particles are launched in steps of about $0.5\sigma$, and the plot range extends over about $\pm 4\sigma$. The energy offset is zero.

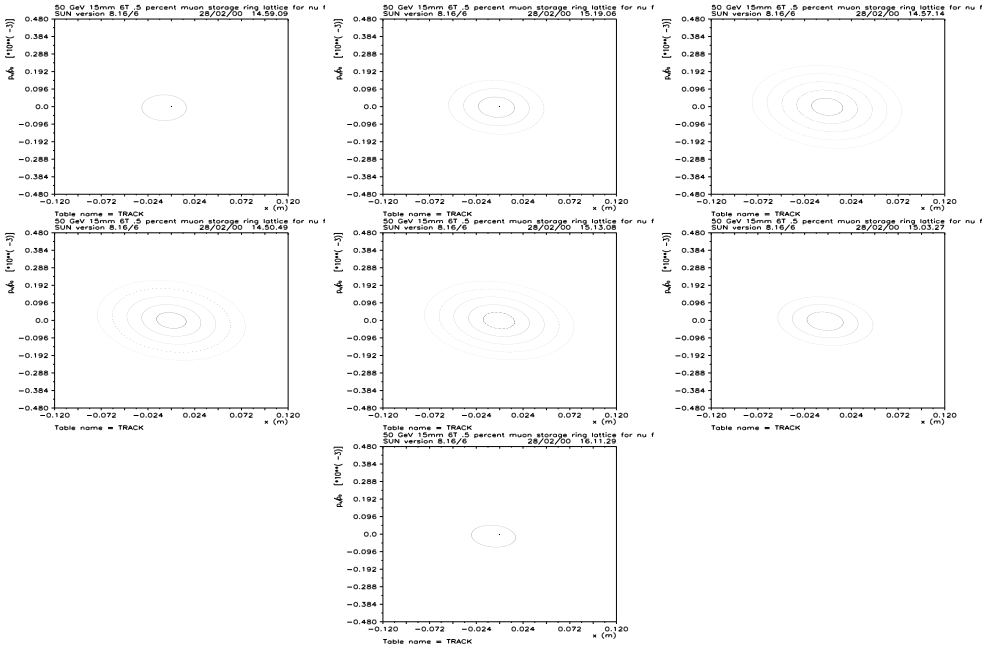

Figure 32: Horizontal phase space for different energy offsets, ranging from $-1.5\%$ to $+1.5\%$ in steps of 1%, as calculated by MAD for the CERN optics. Fringe fields are not included. Each plot extends over $\pm 4$ $\sigma$. Every turn is displayed.

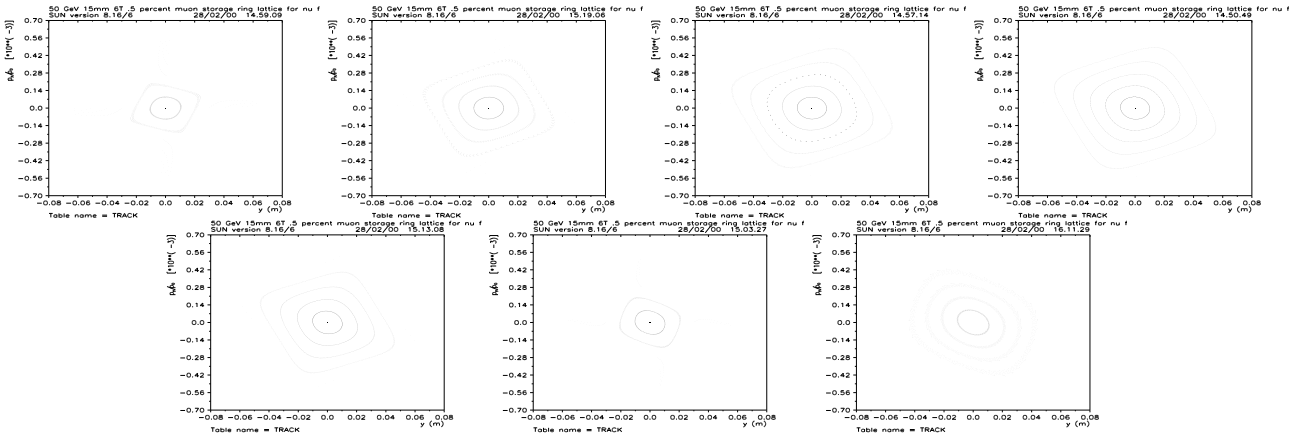

Figure 33: Vertical phase space for different energy offsets, ranging from $-1.5\%$ to $+1.5\%$ in steps of 1%, as calculated by MAD for the CERN optics. Fringe fields are not included. Each plot extends over $\pm 4\ \sigma$. Every turn is displayed.

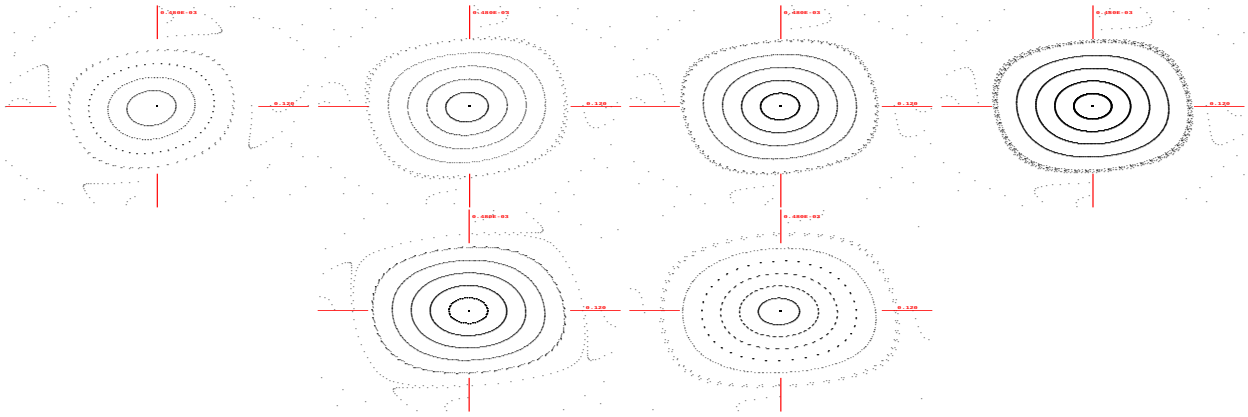

Figure 34: Horizontal phase space for different energy offsets, ranging from $-1.5\%$ to $+1.5\%$ in steps of 1%, as calculated by 7th order 3-dimensional tracking with COSY for the CERN optics. Fringe fields are included except for the matching quadrupoles. Each plot extends over $\pm 4\ \sigma$. Every turn is displayed.

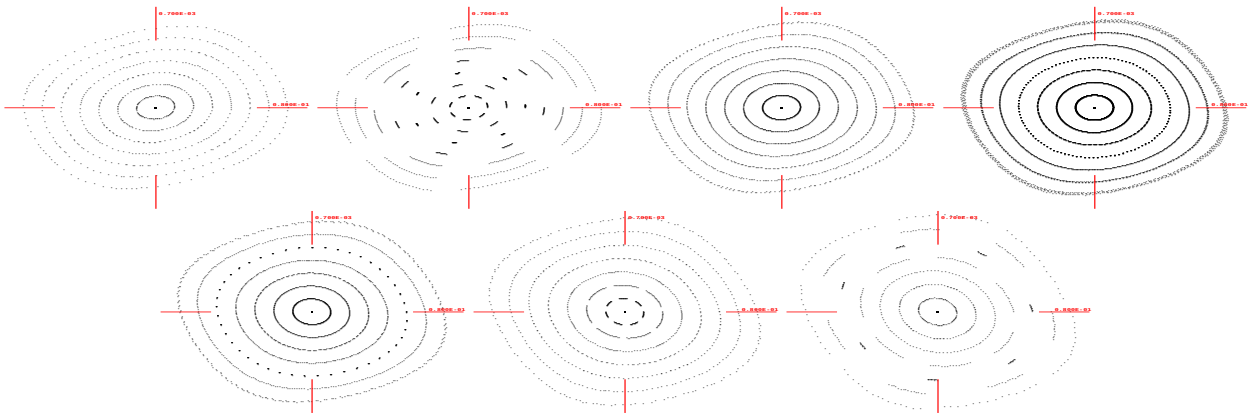

Figure 35: Vertical phase space for different energy offsets, ranging from $-1.5\%$ to $+1.5\%$ in steps of 1%, as calculated by 7th order 3-dimensional tracking with COSY for the CERN optics. Fringe fields are included except for the matching quadrupoles. Each plot extends over $\pm 4\ \sigma$. Every turn is displayed.

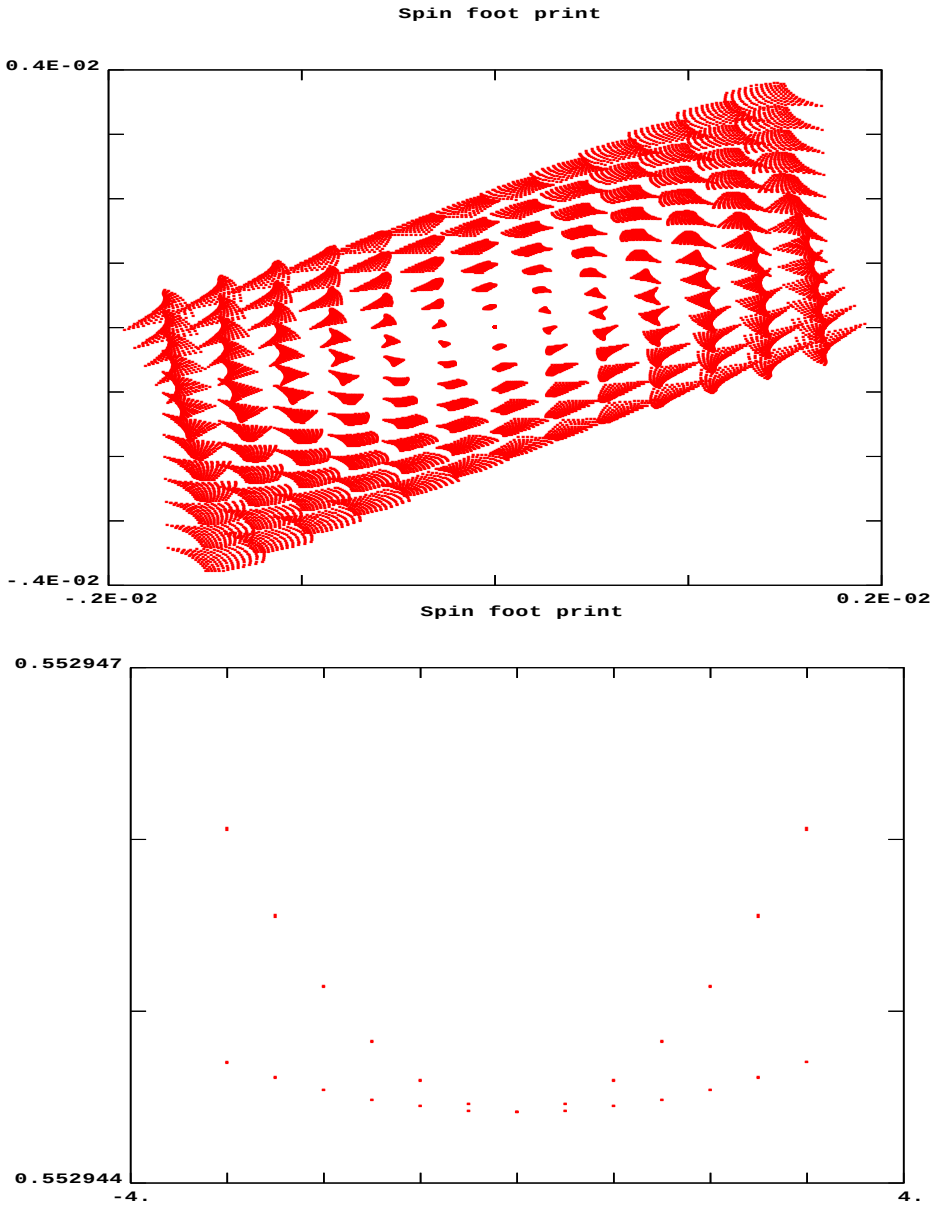


Figure 36: Spin footprints for the CERN storage ring. Shown are the longitudinal and vertical components of the $n$-axis for various transverse coordinates up to $3\sigma$ (left) and the spin tune as a function of starting coordinates in units of $\sigma$ (right). The spin calculations were performed to 3rd order.

# 4 Conclusions

Quadrupole fringe fields in the matching sections between arcs and straights reduce the dynamic aperture to about $1.5\sigma$ for both the FNAL and CERN optics. We expect that the use of weaker and longer quadrupoles in these regions will eliminate the problem. This was demonstrated for the CERN optics. If fringe fields are only taken into account in the rest of the ring, the minimum dynamic aperture increases to about $2.5\sigma$. It is now dominated by the chromatic-correction sextupoles. Tune scans show that the nominal working points are close to optimum, except for the horizontal tune in the CERN optics, which should be separated further from the quarter integer resonance. We tried to improve the performance by adding sextupole or octupole correctors, in order to either cancel the tune shift with amplitude or to reduce the norm of the map. Unfortunately, none of these correction schemes increased the dynamic aperture. We also showed that spin decoherence due to the variation of $n$ axis and spin tune with transverse coordinates will depolarise the muon beam by less than 1%. All the results presented in this report were obtained using the code COSY INFINITY [3, 4].

# 5 Acknowledgements

We would like to thank N. Holtkamp, E. Keil, and F. Ruggiero for helpful discussions and for encouraging this collaboration. This work was supported in parts by the US Department of Energy under contract No. DE-AC02-76HO3000.

# References

[1] M. Berz, K. Makino, B. Erdelyi, "Fringe Field Effects in Muon Rings", Proc. of HEMC'99 workshop on muon colliders at highest energies, Montauk, Long Island (1999).

[2] C. Johnstone, unpublished.

[3] M. Berz et al., COSY INFINITY web page. http://cosy.nscl.msu.edu

[4] K. Makino and M. Berz, "COSY INFINITY version 8", NIM A 427, p. 338 (1999).

[5] K. Brown and J. Spencer, "Non-linear Optics for the Final Focus of the Single-Pass Collider", IEEE Tr. N. Sc. NS-28, 3, p. 2568 (1981).

[6] C. Johnstone, "Large Accetance 50-GeV Muon Storage Ring for Neutrino Production: Lattice Design, CJ2.0" (2000).

[7] The MAD-to-COSY converter was written by R. Servranckx.

[8] F. Zimmermann, "Tune Shift with Amplitude Induced by Quadrupole Fringe Fields", unpublished (2000).

[9] R. Raja, "The effect of RF on polarization in a muon storage ring", unpublished (2000).

[10] E. Keil, private communications, and talk on FNAL work, at keil/MuMu/Doc/NFWG/03dec99.pdf